JGR Oceans

RESEARCH ARTICLE
10.1029/2020JC016773

A Numerical Study of Onshore Ripple Migration Using a Eulerian Two-phase Model

Ali Salimi-Tarazouj[1], Tian-Jian Hsu[1], Peter Traykovski[2], Zhen Cheng[3], and Julien Chauchat[4]

[1]Center for Applied Coastal Research, Civil and Environmental Engineering, University of Delaware, Newark, DE, USA, [2]Applied Ocean Physics and Engineering, Woods Hole Oceanographic Institution, Woods Hole, MA, USA, [3]Convergent Science, Inc., Madison, WI, USA, [4]University of Grenoble Alpes, LEGI, Grenoble, France

Key Points:

- A Eulerian two-phase flow model is utilized to simulate the full profiles of ripple dynamics
- Under an onshore velocity-skewed flow, model results confirm offshore-directed suspended load while the near-bed load forces the onshore ripple migration
- Onshore ripple migration is caused by more intense near-bed sediment flux during the onshore flow cycle and sediment avalanching

Correspondence to:
A. Salimi-Tarazouj,
alisalim@udel.edu

Citation:
Salimi-Tarazouj, A., Hsu, T.-J., Traykovski, P., Cheng, Z., & Chauchat, J. (2021). A numerical study of onshore ripple migration using a Eulerian two-phase model. *Journal of Geophysical Research: Oceans*, *126*, e2020JC016773. https://doi.org/10.1029/2020JC016773

Received 5 SEP 2020
Accepted 23 DEC 2020

Abstract A new modeling methodology for ripple dynamics driven by oscillatory flows using a Eulerian two-phase flow approach is presented in order to bridge the research gap between near-bed sediment transport via ripple migration and suspended load transport dictated by ripple induced vortices. Reynolds-averaged Eulerian two-phase equations for fluid phase and sediment phase are solved in a two-dimensional vertical domain with a k-ε closure for flow turbulence and particle stresses closures for short-lived collision and enduring contact. The model can resolve full profiles of sediment transport without making conventional near-bed load and suspended load assumptions. The model is validated with an oscillating tunnel experiment of orbital ripple driven by a Stokes second-order (onshore velocity skewed) oscillatory flow with a good agreement in the flow velocity and sediment concentration. Although the suspended sediment concentration far from the ripple in the dilute region was underpredicted by the present model, the model predicts an onshore ripple migration rate that is in very good agreement with the measured value. Another orbital ripple case driven by symmetric sinusoidal oscillatory flow is also conducted to contrast the effect of velocity skewness. The model is able to capture a net offshore-directed suspended load transport flux due to the asymmetric primary vortex consistent with laboratory observation. More importantly, the model can resolve the asymmetry of onshore-directed near-bed sediment flux associated with more intense boundary layer flow speed-up during onshore flow cycle and sediment avalanching near the lee ripple flank which force the onshore ripple migration.

Plain Language Summary Sand ripples are common small-scale seafloor bathymetric features in wave-dominant environments. The presence of sand ripples is a major source of bottom friction of overlaying waves and currents. Migration of sand ripples is also a major form of sediment transport shaping large-scale coastal morphological evolution. As waves approach the shore, their shape evolves into sharper crests and broader troughs. This results in fast onshore velocities with a duration of less than half the wave period under the crest and slower offshore velocities under the trough with a duration longer than half the wave period. This process is quantified by a parameter referred to as velocity skewness. While field and laboratory observations reveal a clear relationship between wave orbital velocity skewness and sediment transport through a complex interplay between suspended sand transport above the ripple and ripple migration, the mechanisms driving ripple migration associated with wave orbital velocity skewness remain unclear. This study utilized a new numerical modeling tool, based on the Eulerian two-phase flow methodology, to resolve the full profile of sediment transport to bridge the gap between near-bed sand transport via ripple migration and suspended sand transport dictated by ripple induced vortices. Model results indicate that onshore ripple migration driven by onshore velocity-skewed wave orbital velocity is caused by more intense near-bed sediment flux during onshore flow cycle and sediment avalanching at lee-side of the ripple flank.

1. Introduction

Bedforms with a wide range of geometries and sizes are ubiquitous in the coastal environment when near-bed flows driven by the wave and current exceed the threshold to mobilize sediment particles. Various scales of bedforms can be classified in terms of their length (λ) and height (η). Tidally reversing mega-ripples are observed in inlets and river mouths (e.g., Jones & Traykovski, 2019; Sherwood & Creager, 1990) with a length of several meters. Nearshore mega-ripples (Gallagher, 2003) often exist in energetic surf zones are

observed to be as large as a few meters. During the storm condition, the combined action of the oscillatory flow and the currents (e.g., wave-induced current and tidal current) in the nearshore and continental shelf regions causes the formation and migration of bedforms (Amos et al., 1988; Wengrove et al., 2018). Wengrove et al. (2018) observed that the combined effect of wave and current significantly influence the resulting ripple geometry, orientation, and migration speed and direction. However, the most commonly observed coastal bedforms are wave-driven ripples (Clifton & Dingler, 1984) with a typical length of several tens of centimeters. Accordingly, the formation and evolution timescales of these bedforms can also range from minutes to hours. Among them, wave-driven ripples have been the center of interest among researchers for decades. These dynamic morphological features directly interact with wave bottom boundary layer flow and play a central role in the seabed roughness and net onshore/offshore sediment transport.

Field observations and laboratory studies reveal that the ripple length and height (or steepness) are a function of sediment characteristics and hydrodynamics. Many empirical ripple geometry predictors have been developed (e.g., Clifton, 1976; Mogridge et al., 1994; Nielsen, 1981; O'Donoghue et al., 2006; Wiberg & Harris, 1994) mainly using sediment size (D_{50}), the wave period (T), and the orbital velocity amplitude (U_0). A complete reviews of these ripple predictors are provided by, for example, Nelson et al. (2013). Bagnold and Taylor (1946) identified two types of wave-generated ripples, namely the "grain rolling ripples" and the "vortex ripples." The steepness η / λ of the grain rolling ripples is very small as their height is about a few grain diameters. By increasing either the orbital velocity amplitude or wave period, or collectively increasing the orbital excursion length $\left(d_0 = U_0 T / \pi\right)$, the ripples grow longer and taller and vortices start to form due to flow separation. The vortices change the boundary layer structure by their organized convective motion and suspend a significant amount of sediment into the water column. Clifton (1976) categorized the vortex ripples by using ripple length, orbital excursion length and grain size into three regimes. The "orbital ripples" have their length proportional to orbital excursion length (i.e., $\lambda = \alpha d_0$, α is a constant) with a constant ripple steepness of 0.17. "Suborbital ripples" have their length depending on both grain size and the orbital excursion length. The length of "anorbital ripples" is only proportional to sediment size (e.g., $\lambda = 400 - 600 D_{50}$) and independent of orbital excursion length.

When ripple steepness is greater than about 0.1, vortices are generated due to flow separation (e.g., Hurther & Thorne, 2011). The understanding of the vortex dynamic is crucial for sediment transport and kinetic energy dissipation over vortex ripples. Many experimental studies were conducted over fixed and artificial ripple beds to understand the vortex dynamics (e.g., Du Toit & Sleath, 1981; Earnshaw & Greated, 1998). At the beginning of each half flow cycle, the lee-side vortex starts to grow over the ripple flank and reaches its maximum strength at about the time of maximum free-stream flow. Later, during the flow deceleration phase, the vortex starts to move away from the bed toward the ripple crest. At the time of flow reversal, the vortex is ejected and carried over the ripple crest toward the opposite side until it is fully dissipated. Concurrent with the above-mentioned laboratory experiments, theoretical and numerical modeling studies have been conducted (e.g., Blondeaux & Vittori, 1991; Longuet-Higgins, 1981). By using an inviscid discrete vortex method, Longuet-Higgins (1981) showed the periodic formation-ejection of vortices above the fixed rippled bed. Later, Blondeaux and Vittori (1991) carried out direct numerical simulation for laminar flow over ripples and confirmed the existence of a primary vortex every half cycle, however, they also identified the secondary vortex underneath the primary vortex due to the recirculating flow interacts with the ripple's surface. The vortex pair plays a key role in the subsequent vortex ejection and the formation of the primary vortex on the opposite side of the ripple.

Although these earlier studies lead to a better understanding of the general vortex/vorticity dynamics, the fact that the ripple beds were fixed ignores the dynamic coupling of hydrodynamic and sediment transport which controls the ripple morphodynamics. For instance, the three-dimensional (3D) numerical simulations reported by Barr et al. (2004) showed that the vorticity field varied significantly for different rippled bed shapes, suggesting that the mechanism by which the ripples maintain their shape is a form of dynamic equilibrium. By changing the flow condition, a movable ripple bed must adjust its shape to a new equilibrium state. There are several experimental (e.g., Doucette & O'Donoghue, 2006) and field (e.g., Traykovski et al., 1999) studies documenting how the ripples evolve into a new equilibrium state due to changing flow condition. van der Werf et al. (2007) reported detailed measurements of velocities, suspended sand concentrations, and ripple migration rate over full-scale orbital ripples in oscillatory flow. By utilizing the

cross-correlation PIV system, they measured the asymmetric and symmetric vortex generation and shedding over the mobile ripple bed under second-order Stokes (onshore velocity-skewed) and sinusoidal oscillatory flows, respectively. They showed that the velocity skewness (asymmetry in velocity magnitude between positive and negative wave phases) causes asymmetric ripple geometry and vortex generation. Therefore, boundary layer flow, sediment transport, ripple geometry, and migration are all interrelated processes. A more thorough analysis of the vorticity dynamic and vortex formation-ejection over full-scale ripples can be found in the recent work of Yuan and Wang (2019). By analyzing velocity, vorticity, and swirling length (Zhou et al., 1999) simultaneously, they revealed the similar pair-vortex pattern previously only observed in direct numerical simulation (Blondeaux & Vittori, 1991; Önder & Yuan, 2019).

Due to asymmetric vortex generation and ejection over the ripple under velocity-skewed oscillatory flow, van der Werf et al. (2007) further showed that the net (time and ripple-averaged) suspended flux is offshore directed. On the other hand, the measured total net sand transport was either onshore directed or much less offshore directed, suggesting that a significant amount of onshore transport occurred as ripple migration. However, processes driving the near-bed load transport associated with vortex dynamics subjected to asymmetric flow motion and onshore ripple migration were not reported because the concentrated region of sediment transport cannot be directly measured. The importance of ripple migration and near-bed load (or called bedload) transport flux have been raised by several field observations and wave flume experiments (e.g., Crawford & Hay, 2001; Hurther & Thorne, 2011; Rodriguez-Aboudo & Foster, 2014; Traykovski et al., 1999). Since the net transport is a subtle balance between onshore directed near-bed load transport and offshore-directed suspended load transport, it becomes a main challenge in both measurement and modeling. According to extensive field observations, Traykovski et al. (1999) hypothesized that the ripple geometry and ripple regimes depend on the ratio of suspended load to bedload during transport. They argued that the existence of longer wavelength ripples at longer wave periods is because the lower velocities associated with longer-period waves (under the same wave orbital diameter) encourages more near-bed load transport via ripple migration. On the contrary, the suspended load may be dominant for shorter-period waves with higher velocities. This difference may also affect the transition of ripple regimes since the near-bed load is more conducive to orbital scale ripples, while fully suspended transport favors anorbital ripples or the sheet flow condition. In the literature, several researchers tried to relate the ripple type to the ratio of bedload to suspended load. For instance, Wiberg and Harris (1994) used the Rouse number $P_{sf} = w_s / \kappa u_*$ which is the ratio of sediment settling velocity (w_s) to bed shear velocity (u_*) with von Karman constant $\kappa = 0.41$. Similar nondimensional parameters, often called vortex suspension parameter or phase-lag parameter for ripple bed have also been suggested by van der Werf et al. (2006) and Ribberink et al. (2008), respectively.

Complex processes related to sediment transport over sand ripples (e.g., vortex generation, ejection, and shedding) and ripple bed dynamics (e.g., ripple formation, evolution, and migration) pose challenges to numerical modeling. One of the key challenges is a complete description of sediment transport and bathymetry evolution. Marieu et al. (2008) utilized Dune2D (Tjerry & Fredsøe, 2005) to model wave-driven sediment transport and ripple evolution with promising results. Dune2D solves Reynolds-averaged Navier-Stokes (RANS) equations with $k - \omega$ closure for 2D vertical (2DV) flow and suspended sediment transport. Moreover, an empirical bedload model based on Mayer-Peter and Muller formula was included and the morphological evolution was solved by the Exner equation. They demonstrated the model's capability to simulate a range of ripple evolution processes such as merging, sliding, and splitting. Since turbulent flow over ripples involves complex vortices, another model challenge is the accuracy of two-equation closure in RANS models. To resolve turbulence coherent structures over ripples more accurately, the large-eddy simulation (LES) approach has been utilized by several studies (e.g., Chang & Scotti, 2003; Chou & Fringer, 2010; Dimas & Leftheriotis, 2019; Zedler & Street, 2006). In particular, Dimas and Leftheriotis (2019) validated the simulation results for flow velocity and suspended sediment concentration with measured data reported by van der Werf et al. (2007) with good agreements. However, when turbulence is much accurately resolved by LES, it appears that the conventional suspended load and bedload formulation utilizing empirical formula for reference concentration and bedload transport cause an overestimate of the ripple evolution/migration speed (Chou & Fringer, 2010).

To avoid the bedload/suspended load assumptions, Penko et al. (2011) applied a 3D mixture model to study ripple evolution. The sediment-fluid mixture is treated as a single continuum with mixture properties de-

pending on sediment concentration and flow shear rate. More recently, high fidelity two-phase simulations with LES for fluid phase, coupled with discrete element model (DEM) for particle phase were reported by Finn et al. (2016). They show that the two-phase LES-DEM approach can successfully simulate sediment transport and ripple migration under oscillatory flow for a single equilibrium ripple. Although this type of Euler-Lagrange approach can accurately model the complex particle-particle interactions and particle-fluid interactions, the applications to long timescale and large domain simulations are restricted at the moment due to high computational cost.

The Eulerian-Eulerian two-phase modeling approach can also be used to model full profiles of sediment transport without suspended load/near-bed load assumptions. Since the particle phase is modeled as a continuum through statistical averaging, it is also much more computationally efficient than the Euler-Lagrange approach and hence allowing a wider range of ripple modeling applications. However, due to the averaging over particles, more closure assumptions on particle-phase stress and turbulence-particle interaction are needed. The Eulerian two-phase modeling approach has been used extensively to model Reynolds-averaged 1D vertical sheet flows (e.g., Cheng et al., 2017; Dong & Zhang, 1999; Li et al., 2008) and sheet flow measured in wave flumes (Kim et al., 2018). More recently its capability has been extended to 3D LES (Cheng et al., 2018). Chen and Yu (2015) used this approach to simulate sediment transport over 2D fixed vortex ripples. The model was validated with laboratory data for velocity and suspended sediment concentration reported by van der Werf et al. (2007). The model is able to simulate the primary and secondary vortex generation-ejection process, although they do not extend the model's capability for ripple migration and hence the total load transport cannot be investigated.

In this paper, we present a new modeling methodology for full sediment transport dynamics in the ripple mode using a Eulerian two-phase flow approach to bridge the research gap between near-bed sediment transport via ripple migration and suspended load transport dictated by ripple induced vortices. We extend the Eulerian two-phase model, SedFoam (Chauchat et al., 2017; Cheng et al., 2017), which has been validated extensively for sheet flows, to simulate sediment transport and ripple migration using a turbulence-averaged 2DV formulation. For this purpose, we validated SedFoam with laboratory experiments reported by van der Werf et al. (2007). We then focus on the analyses of the intrawave characteristics of the flow field and sediment fluxes, and spatially averaged and/or wave-period-averaged fields to gain insight into how the flow asymmetry, vortices generation, and evolution can drive the ripple migration via onshore-directed near-bed load transport and offshore-directed suspended load transport. The remaining of this paper is organized as follows. In Section 2, the model formulation is presented. Section 3 discusses model setup and model results are presented in Section 4. Concluding remarks are given in Section 5.

2. Model Formulation

The Eulerian two-phase model, SedFoam (Chauchat et al., 2017; Cheng et al., 2017) has been extended to simulate wave orbital ripples driven by oscillatory flows. SedFoam is an open-source model for sediment transport applications developed in the OpenFOAM framework. The two-phase formulation allows seamless integration of turbulence, particle-fluid, particle-particle interactions, and seabed dynamics into a single modeling framework and thus avoid artificial separation of transport into near-bed load and suspended load layers. We adopt the version of SedFoam described in Chauchat et al. (2017) and as a first step, the Reynolds-averaged formulation with k-ε turbulence closure model is used. The oscillatory flow is generated in the streamwise (x) direction (direction perpendicular to the ripple crest), while the ripples are assumed to be homogeneous in the spanwise direction and a 2DV model domain describing turbulence-averaged processes in the xz-plane is established (see Figure 1).

In the Reynolds-averaged Eulerian two-phase flow formulation, both the fluid (water) phase and dispersed particulate (sediment) phase are modeled as a continuum. The mass conservation equations for fluid and sediment phases can be written as:

$$\frac{\partial\left(1-\phi\right)}{\partial t}+\frac{\partial\left(1-\phi\right)u_i^f}{\partial x_i}=0 \tag{1}$$

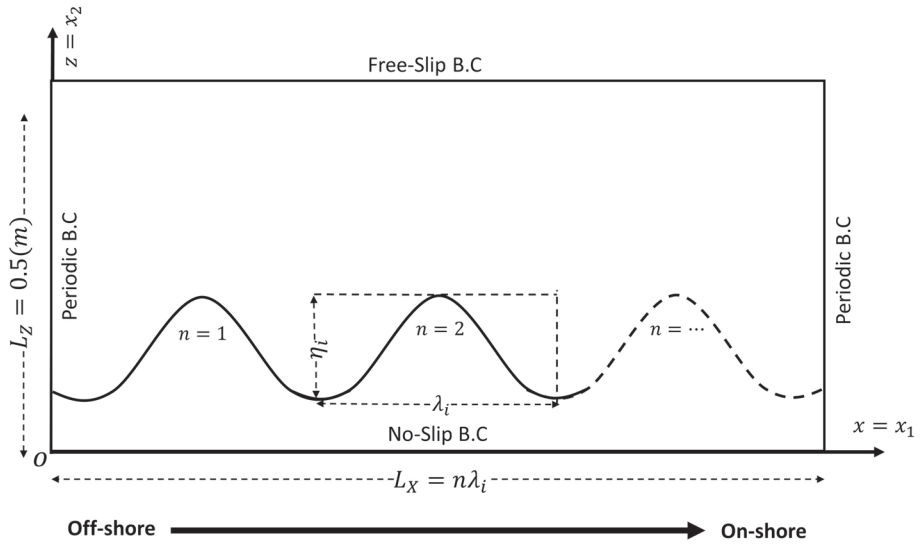

Figure 1. Schematic plot of the model domain and the initial ripple bed.

$$\frac{\partial \phi}{\partial t} + \frac{\partial \phi u_i^s}{\partial x_i} = 0 \tag{2}$$

where $i = 1, 3$ represents streamwise and vertical directions, respectively, and ϕ is the sediment volumetric concentration, u_i^f is fluid velocity and u_i^s is sediment velocity. The momentum equations for fluid and sediment phases are expressed as:

$$\frac{\partial \rho^f (1-\phi) u_i^f}{\partial t} + \frac{\partial \rho^f (1-\phi) u_i^f u_j^f}{\partial x_j} = -(1-\phi)\frac{\partial P^f}{\partial x_i} + (1-\phi) f_i + \frac{\partial \tau_{ij}^f}{\partial x_j} - \rho^f (1-\phi) g \delta_{i3} + M_i^{fs} \tag{3}$$

$$\frac{\partial \rho^s \phi u_i^s}{\partial t} + \frac{\partial \rho^s \phi u_i^s u_j^s}{\partial x_j} = -\phi \frac{\partial P^f}{\partial x_i} + \phi f_i - \frac{\partial P^s}{\partial x_i} + \frac{\partial \tau_{ij}^s}{\partial x_j} - \rho^s \phi g \delta_{i3} + M_i^{sf} \tag{4}$$

where $\rho^f = 1000\left(kg / m^3\right)$ and $\rho^s = 2650\left(kg / m^3\right)$ are fluid and sediment density, $g = -9.81$ m/s^2 is the gravitational acceleration and P^f is the fluid pressure. The external pressure gradient that drives the flow is represented by f_i. The fluid stress τ_{ij}^f includes the grain-scale (viscous) stress and the turbulent Reynolds stress, which are modeled by the k-ε turbulence model. The shear-driven particle normal stress P^s and shear stress τ_{ij}^s also, require closures to be discussed in more detail later. Finally, M_i^{fs} and M_i^{sf} represent the interphase momentum transfer between the fluid and particle phase, and $M_i^{fs} = -M_i^{sf}$ follows Newton's third law. In this study, the momentum exchange of the fluid phase and particle phase is modeled as:

$$M_i^{fs} = -\phi\beta\left(u_i^f - u_i^s\right) + \beta \frac{\nu^{ft}}{\sigma_c} \frac{\partial \phi}{\partial x_i} \tag{5}$$

The two terms on the right-hand side (RHS) are due to drag force with β as the drag parameter. The first term represents averaged drag force due to the mean velocity difference between fluid and particle phases. The second term is the fluid turbulent suspension, which results from the correlation of sediment concentration and fluid velocity fluctuations. The gradient transport assumption was adopted here with turbulent eddy viscosity ν^{ft} to be calculated by a two-equation closure model and the Schmidt number $\sigma_c = 1$ is used for simplicity. Other forces, such as added mass forces and lift forces are neglected for simplicity as they have

been shown to play a minor role in Reynolds-averaged formulation (Jha & Bombardelli, 2010). The drag parameter β, is modeled by following Ding and Gidaspow (1990). At lower concentration ($\phi < 0.2$), the model modifies the drag on an isolated sphere by a hindered settling factor to account for the neighboring particles. For dense sediment concentration ($\phi \geq 0.2$), the model recovers the equation for flow through static packed beds (Darcy law). Hence, the drag parameter formulation implemented as,

$$\beta = \begin{cases} \dfrac{150\phi\nu^f\rho^f}{(1-\phi)d^2} + \dfrac{1.75\rho^f\left|u^f - u^s\right|}{d}, \phi \geq 0.2 \\ \dfrac{1.75C_d\rho^f\left|u^f - u^s\right|(1-\phi)^{-1.65}}{d}, \phi < 0.2 \end{cases} \tag{6}$$

where d is the sediment diameter and the drag coefficient C_d is calculated as:

$$C_d = \begin{cases} \dfrac{24\left(1 + 0.15\mathrm{Re}_p^{0.687}\right)}{\mathrm{Re}_p}, \mathrm{Re}_p \leq 1000 \\ 0.44, \qquad\qquad \mathrm{Re}_p > 1000 \end{cases} \tag{7}$$

in which $Re_p = (1-\phi)\left|u^f - u^s\right| d / \nu^f$ is the particle Reynolds number, and ν^f is the fluid molecular viscosity.

The fluid stress (τ_{ij}^f) consists of turbulent Reynolds stress R_{ij}^{ft} and grain-scale fluid stresses r_{ij}^f. We assume grain-scale stress is mainly due to viscous stress and fluid-particle interaction at the grain scale is ignored in this study. Hence, the equation for fluid stress is written as:

$$\tau_{ij}^f = R_{ij}^{ft} + r_{ij}^f = \rho^f(1-\phi)\left[\left(\upsilon^{ft} + \upsilon\right)\left(\frac{\partial u_i^f}{\partial x_j} + \frac{\partial u_j^f}{\partial x_i} - \frac{2}{3}\frac{\partial u_k^f}{\partial x_k}\delta_{ij}\right) - \frac{2}{3}k^f\delta_{ij}\right] \tag{8}$$

in which the turbulence eddy viscosity υ^{ft} is calculated by turbulent kinetic energy (TKE; k^f) and its dissipation rate (ε^f) as

$$\upsilon^{ft} = C_\mu\frac{\left(k^f\right)^2}{\varepsilon^f} \tag{9}$$

where $C_\mu = 0.09$ is an empirical coefficient. The TKE k^f is calculated by its balance equation written as (Cheng et al., 2017)

$$\begin{aligned} \frac{\partial k^f}{\partial t} + u_j^f\frac{\partial k^f}{\partial x_j} &= -\frac{Re_{ij}^{ft}}{\rho^f}\frac{\partial u_i^f}{\partial x_j} + \frac{\partial}{\partial x_j}\left[\left(\nu^f + \frac{\nu^{ft}}{\sigma_k}\right)\frac{\partial k^f}{\partial x_j}\right] - \epsilon^f - \frac{2\beta(1-\alpha)\phi k^f}{\rho^f(1-\phi)} \\ &\quad - \frac{1}{(1-\phi)}\frac{\nu^{ft}}{\sigma_c}\frac{\partial\phi}{\partial x_j}(s-1)g_j \end{aligned} \tag{10}$$

The last term in Equation 10 represents the modulation of TKE due to density stratification and the penultimate term is the attenuation of TKE through drag in which α is introduced to characterize the degree of correlation between sediments and fluid velocity fluctuations. Since turbulent fluctuation is not directly resolved, α is parameterized empirically as

$$\alpha = e^{-B.St} \tag{11}$$

where $B = 0.22$ is used by calibrating with extensive sheet flow data (Cheng et al., 2017). This empirical formulation allows α varies between 0 and 1, depending on the degree of correlation between particles and fluid velocity fluctuations quantified by the Stokes number St:

$$St = \frac{t_p}{t_l} \tag{12}$$

where $t^p = \rho^s / \left(\beta\left(1-\phi\right)\right)$ is particle response time and $t_l = k^f / \left(6\varepsilon^f\right)$ is the characteristic timescale of energetic eddies. The balance equation for the rate of TKE dissipation ε^f is written as

$$\begin{aligned}\frac{\partial \epsilon^f}{\partial t} + u_j^f \frac{\partial \varepsilon^f}{\partial x_j} &= -C_{1\epsilon}\frac{\epsilon^f}{k^f}\frac{R_{ij}^{ft}}{\rho^f}\frac{\partial u_i^f}{\partial x_j} + \frac{\partial}{\partial x_j}\left[\left(\nu^f + \frac{\nu^{ft}}{\sigma_\epsilon}\right)\frac{\partial \epsilon^f}{\partial x_j}\right] - C_{2\epsilon}\frac{\epsilon^f}{k^f}\epsilon^f \\ &\quad -C_{3\epsilon}\frac{\epsilon^f}{k^f}\frac{2\beta\left(1-\alpha\right)\phi k^f}{\rho^f\left(1-\phi\right)} - C_{4\epsilon}\frac{\epsilon^f}{k^f}\frac{1}{\left(1-\phi\right)}\frac{\nu^{ft}}{\sigma_c}\frac{\partial \phi}{\partial x_j}\left(s-1\right)g_j\end{aligned} \tag{13}$$

Following Cheng et al. (2017), we use $C_{1\epsilon} = 1.44, C_{2\epsilon} = 1.92, C_{3\epsilon} = 1.2, \sigma_k = 1.0, \sigma_\epsilon = 1.3,\ \sigma_c = 1.0,$ and $C_{4\epsilon} = 0$ or 1 for stable and unstable density stratification, respectively.

Particle stresses are assumed to be dominated by binary collisions in dilute and moderate concentration driven by high flow shear. However, when sediment concentration is higher than the random-loose packing threshold of 0.57, flow shear becomes negligible and particle stress is mainly caused by enduring contact. Both particle pressure (P^s) and particle shear stress (τ_{ij}^s) consist of a collisional component and an elastic/frictional contact component distinguished by superscripts "sc" and "sf," respectively:

$$P^s = P^{sc} + P^{sf} \tag{14}$$

$$\tau_{ij}^s = \tau_{ij}^{sc} + \tau_{ij}^{sf} \tag{15}$$

In this study, we adopt the kinetic theory of granular flow for collisional component based on the granular temperature, Θ, which is defined as one-third of the kinetic energy of particle velocity fluctuation. The balance equation for granular temperature is written as (Ding & Gidaspow, 1990; Hsu et al., 2004):

$$\frac{3}{2}\left[\frac{\partial \rho^s\left(\phi\right)\Theta}{\partial t} + \frac{\partial \rho^s\left(\phi\right)\Theta u_j^s}{\partial x_j}\right] = \left(-P^{sc}\delta_{ij} + \tau_{ij}^{sc}\right)\frac{\partial u_i^s}{\partial x_j} - \frac{\partial q_j}{\partial x_j} - \gamma_s + J_{\text{int}} \tag{16}$$

where the terms in RHS are the production of granular temperature, the gradient of granular temperature flux, q_j, dissipation of rate due to the inelastic collision γ_s and dissipation or production of granular temperature due to fluid phase, suggested by Hsu et al. (2004) as $J_{int} = \phi\beta\left(2\alpha k^f - 3\Theta\right)$. More detail about the closures for different terms in the RHS of Equation 16 is provided by Cheng et al. (2017). The particle pressure due to enduring contact in the highly concentrated region is calculated following Johnson et al. (1990) to model elastic behavior in low loading condition:

$$P^{sf} = \begin{cases} 0, & \phi < 0.57 \\ F\dfrac{\left(\phi - 0.57\right)^3}{\left(0.635 - \phi\right)^5}, & \phi \geq 0.57 \end{cases} \tag{17}$$

with $F = 0.05$ Pa, suggested by Cheng et al. (2017) for the application of sand transport in water. The particle shear stress due to frictional contact in quasistatic (nearly zero shear rate) highly concentrated sediment skeleton is modeled as,

$$\tau_{ij}^{sf} = 2\rho^s \nu_{Fr}^s S_{ij}^s \tag{18}$$

where ν_{Fr}^s is frictional viscosity and $S_{ij}^s = \frac{1}{2}\left(\left[\frac{\partial u_i^s}{\partial x_j} + \frac{\partial u_j^s}{\partial x_i}\right]\right) - \frac{1}{3}\frac{\partial u_k^s}{\partial x_k}\delta_{ij}$ is the deviatoric part of the strain rate of the sediment phase. Srivastava and Sundaresan (2003) suggest that the normal stress and shear stress are related by a frictional angle θ_f in the region of enduring contact and a frictional viscosity is calculated as (Scheaffer, 1987),

$$\nu_{Fr}^{s} = \frac{P^{sf}\sin\left(\theta_f\right)}{\rho^{s}\left(\left|S_{ij}^{s}\right|^{2} + D_{small}^{2}\right)^{1/2}}. \tag{19}$$

We specify $\theta_f = 32^o$ which is close to the angle of repose for cohesion-less sand grains. As will be demonstrated later, this angle is the threshold above which the avalanching of sand grains occurs and it plays an important role in maintaining ripple geometry and migration. Regularization technique (Chauchat & Médale, 2014) is used by introducing D_{small} in Equation 19 to ensure the numerical stability when shear rate becomes zero in highly concentrated sediment bed. As the particle stress is solved by using a mixed explicit-implicit method for computationally efficiency, the maximum sediment viscosity is also limited to be $\left(\nu_{Fr}^{s}\right)_{max} = 10^5$ to ensure numerical stability. More details can be found in Nagel et al. (2020). The formulation of particle pressure and shear stress is essential to capture the transition from fluid-like to solid-like behavior of sediment bed and it is an important element in the present modeling of ripple evolution and migration. The ripple migration rate is sensitive to the bed stiffness which is controlled by the frictional viscosity ν_{Fr} shown in Equation 19. By using $D_{\text{small}} = 10^{-10}$ and $\left(\nu_{Fr}^{s}\right)_{max} = 10^5$ in the present study, the sediment bed became sufficiently stiff to maintain the ripple shape and allows the resulting ripple migration rate agrees very well with measured data (see more discussion in Section 4.3). However, using much larger values of D_{small} and smaller values of $\left(\nu_{Fr}^{s}\right)_{max}$ cause unrealistic ripple slumping while a much smaller D_{small} and larger $\left(\nu_{Fr}^{s}\right)_{max}$ eventually prevents ripple migration.

3. Model Setup

To start the simulation with a stable rippled bed, the sediment concentration profile from a 1DV flat-bed simulation after the flow reaching the equilibrium (Cheng et al., 2017) was mapped to every vertical column of grid points throughout the entire streamwise direction in the domain following the prescribed initial sinusoidal bathymetry by adjusting the vertical location of the profile (see Figure 1). The velocities for sediment and fluid fields are initially set to be zero. This mapping procedure is utilized to establish appropriate initial contact stresses $P^{sf} = f\left(\phi\right)$ and $\tau^{sf} = f\left(P^{sf}\right)$ (see Equations 17–19) in the ripple bed to prevent unrealistic initial slumping.

At the top domain boundary, a free-slip (i.e., Neumann) boundary condition is used for both the fluid and sediment field quantities (see Figure 1). At the bottom boundary of the domain, a no-slip boundary is used for the velocities of both phases while a zero-gradient boundary is used for the other quantities. It is noted that in the present Eulerian two-phase model, the whole profiles of primary variables from the dilute suspension, dense transport, and immobile bed are resolved, and the bottom no-slip boundary of the model domain plays a minor role in the results because it is under a thick layer (at least 5 cm) of immobile sediment bed. For the pressure field, a fixed zero value is specified at the top boundary, and at the bottom boundary of the domain, a zero gradient condition is imposed.

Periodic boundary conditions are specified at the two lateral boundaries to minimize computational domain length and hence computation cost. However, the choice of the periodic boundary condition may limit the development of ripple length. In this study, the initial ripple length λ_i is set to be the same as the measured equilibrium ripple reported by van der Werf et al. (2007). The domain length specified such that includes $n = 3$ ripples (i.e., $L_x = 3\lambda_i$, see Figure 1). For initial ripple height η_i, we specify a much larger value than that measured ripple height. The domain height is set to be $L_z = 0.5$ m in all the simulations. Therefore, as far as ripple geometry is concerned, the model investigation presented in this paper focuses on predicting ripple height (or ripple steepness) and shape.

The oscillatory flow is driven by a prescribed horizontal pressure gradient which generates a free-stream velocity time series following the Stokes second-order wave:

Table 1
Simulated Flow Conditions and Ripple Dimensions With U_1: First Harmonic Amplitude of Free-Stream Velocity, U_2: Second Harmonic Amplitude, U_{rms}: Root-Mean-Square Velocity, R: Velocity Skewness, $\psi = \frac{2U_{rms}^2}{(s-1)gD_{50}}$ Mobility Number, λ and (η / λ): Ripple Height and Steepnes With Subscript e = Experimentally Measured; i = Initial Modeled; f = Final Modeled

Case ID	U_1 (m/s)	U_2 (m/s)	U_{rms} (m/s)	$R = \frac{U_1+U_2}{2U_1}$	ψ	λ_e(m)	$(\eta / \lambda)_e$	λ_i(m)	$(\eta / \lambda)_i$	λ_f(m)	$(\eta / \lambda)_f$
Case 1	0.54	0.095	0.39	0.59	42	0.41	0.19	0.41	0.27	0.41	0.185
Case 2	0.48	0	0.34	0.5	32	0.46	0.17	0.46	0.24	0.46	0.175

$$U_0(t) = U_1 \cos(\omega t) + U_2 \cos(2\omega t + 2\sigma_0) \tag{20}$$

where U_1 and U_2 are the first- and second-order near-bed orbital velocity amplitude and $\omega = 2\pi / T$ is the angular frequency where T represents the wave period. The phase lag, σ_0, is calculated such that the free-stream velocity becomes zero at $t = 0$. To produce an oscillatory sinusoidal flow U_2 is set to zero. In the study, the positive (negative) velocity represents onshore (offshore) directed flow.

The mathematical model described here is solved numerically via SedFoam, which is created using the CFD library of toolbox OpenFOAM (version 2.4.0). For more details about the numerical implementation, the reader is referred to Chauchat et al. (2017).

4. Model Results

Two oscillatory water tunnel experiments for orbital ripple reported by van der Werf et al. (2007) are simulated using SedFoam. Case 1 is to model the experiment Mr5b63 in which the orbital ripple is formed under an onshore velocity-skewed Stokes second-order oscillatory flow. A detailed comparison between model results and measured data is analyzed for this case to validate the model. Case 2 is to model experiment Mr5b50 in which the ripple is forced by a sinusoidal (symmetric) oscillatory flow. The purpose of this simulation is to investigate the difference between ripples under symmetric and asymmetric flows which can lead to a better understanding of intrawave onshore/offshore sediment transport and mechanisms driving ripple migration. In the laboratory experiment, well-sorted coarse sand of a grain size $D_{50} = 0.44$ mm with specific density $s = 2.65$ is utilized and the oscillatory flow period is $T = 5$ s. More information about flow conditions is provided in Table 1 which includes the measured equilibrium ripple length (λ_e) and steepness $(\eta / \lambda)_e$, along with initial and final modeled λ and η / λ using i and f subscripts, respectively. In Case 1, following the measured data, the wave condition gives a ripple length of $\lambda_e = 0.41m$ so the domain length of $L_x = 3 * \lambda_e = 1.23m$ is chosen. For Case 2, the measured ripple length is $\lambda_e = 0.46m$ and the same procedure gives $L_x = 1.38\ m$**.** To test the model's capability to predict the unique equilibrium ripple height, the initial ripple height is set to be $\eta_i = 0.11m$ for both cases, which is significantly larger than the expected equilibrium ripple height of $\eta_e = 0.076m$ and $\eta_e = 0.081m$ for Case 1 and Case 2, respectively. Numerical experiments using different initial ripple height for Case 1, including a case started from a nearly flat bed condition, suggest that the final equilibrium ripple heights are nearly the same, although the timescales to reach the equilibrium are different. The domain height is specified to be 0.5 m which is at least four to five times larger than the ripple height. Model results confirm that this domain height is sufficiently large to have a negligible impact on the modeled boundary layer and ripple process. The computational domain is discretized into $N_x = 2{,}400$ uniform grids in the streamwise direction with a grid length $\Delta x \approx 0.55mm$. In the vertical direction, nonuniform grids of $N_z = 438$ are used, and by keeping the grid ratio near unity $(\frac{\Delta x}{\Delta z} \approx 1)$, $\Delta z \approx 0.5mm$ is specified in the ripple bed and near the ripple's surface and Δz is then gradually increased away from the ripple bed to $\Delta z \approx 3mm$ near the top boundary.

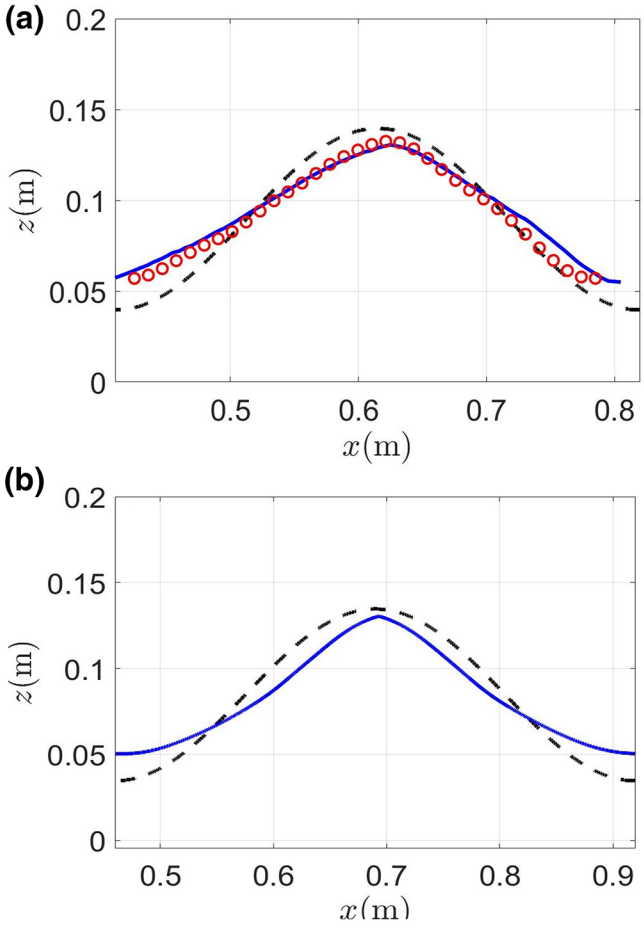

Figure 2. Modeled middle ripple profile at final equilibrium (solid curve) contrasted with initial ripple profile (dashed curve) for Case 1 and Case 2 shown in (a) and (b), respectively. The red symbols in (a) represent the measured ripple profile at equilibrium reported by van der Werf et al. (2007).

In the following subsections, the model results are compared with the measured experimental data for Case 1 (corresponding to experiment Mr5b63) in detail for ripple geometry, time-dependent and averaged quantities, and migration rate. In the rest of the paper, the averaged operator "< >" with subscript *t*, *x*, or *tx* represents time-averaging over wave period, horizontal averaging over the ripple length, or time-horizontal-averaging, respectively.

4.1. Ripple Geometry

After driving the simulations for 18 and 12 wave periods for Case 1 and Case 2, respectively, the ripples evolved into a more realistic shape. The model results discussed next are all based on the last period after the ripple evolution reaches a quasi-equilibrium state for the middle ripple. The quasi-equilibrium state is determined when the calculated wave-period-averaged net transport rate between two consecutive flow period is less than 5%. Figure 2 shows the wave-period averaged ripple profiles (for the middle ripple in the domain) defined as the contour of $\phi = 0.57$, for both Case 1 (Figure 2a) and Case 2 (Figure 2b). We choose a critical concentration of 0.57 to determine the ripple bed profile as it is the theoretical random loose packing concentration for uniform spheres. Model results also suggest that the calculated ripple profile is not sensitive to the small changes in the critical concentration (e.g., use 0.55 or 0.59). The final ripple geometry is compared with measured data for Case 1 (see Figure 2a). The modeled ripple height $\eta_f \approx 0.075m$, which gives a ripple steepness of $\left(\eta / \lambda\right)_f = 0.185$ and it is in good agreement with measured data reported by van der Werf et al. (2007) (see Table 1). The model is also able to reproduce a steeper slope at the onshore (right) side of the ripple, which is consistent with measured data and an expected onshore migration (see more discussion in Section 4.3). On the other hand, for Case 2 driven by sinusoidal wave motion, the equilibrium ripple shape is much more symmetric. Due to symmetric flow, the modeled ripples do not migrate, and the ripple profile is symmetric with $\left(\eta / \lambda\right)_f = 0.175$, which is in good agreement with measured $\left(\eta / \lambda\right)_e = 0.17$. The interrelationship between asymmetric vortices motion, sediment fluxes, and avalanching leading to the asymmetric ripple shape and net migration will be discussed in detail later.

4.2. Time-Dependent Flow

Modeled streamwise velocity profiles at four different horizontal locations of the ripples under eight different instances are shown in Figure 3. The top panel shows the time series of free-stream velocity, which also signifies those time instances for which the comparisons between model results and experimental data are conducted. Modeled streamwise velocities generally show good agreement with measured data. During the off-onshore flow reversal (Figure 3a), near-bed flow at the stoss (offshore) side and the crest of the ripple accelerates with the feature of overshoot velocity near the ripple's surface. The model results show a slightly larger onshore-directed velocity near the ripple's surface than the measured data. Importantly, the model is able to capture the velocity profiles of the primary vortex in the flow separation zone in the lee (onshore) side of the ripple during and after the onshore flow peak (see velocity profile at $x = 0.72$ m in Figures 3b and 3c). During onshore-offshore flow reversal (Figure 3d), the modeled velocity profiles capture the intense offshore-directed flow near the ripple's surface at $x = 0.72$ m (approaching −0.5 m/s) but a slightly lower ejection velocity near the ripple crest comparing with measured data. During the offshore flow peak (Figure 3e), the model predicts a slightly weaker primary vortex in the flow separation zone (velocity profiles at

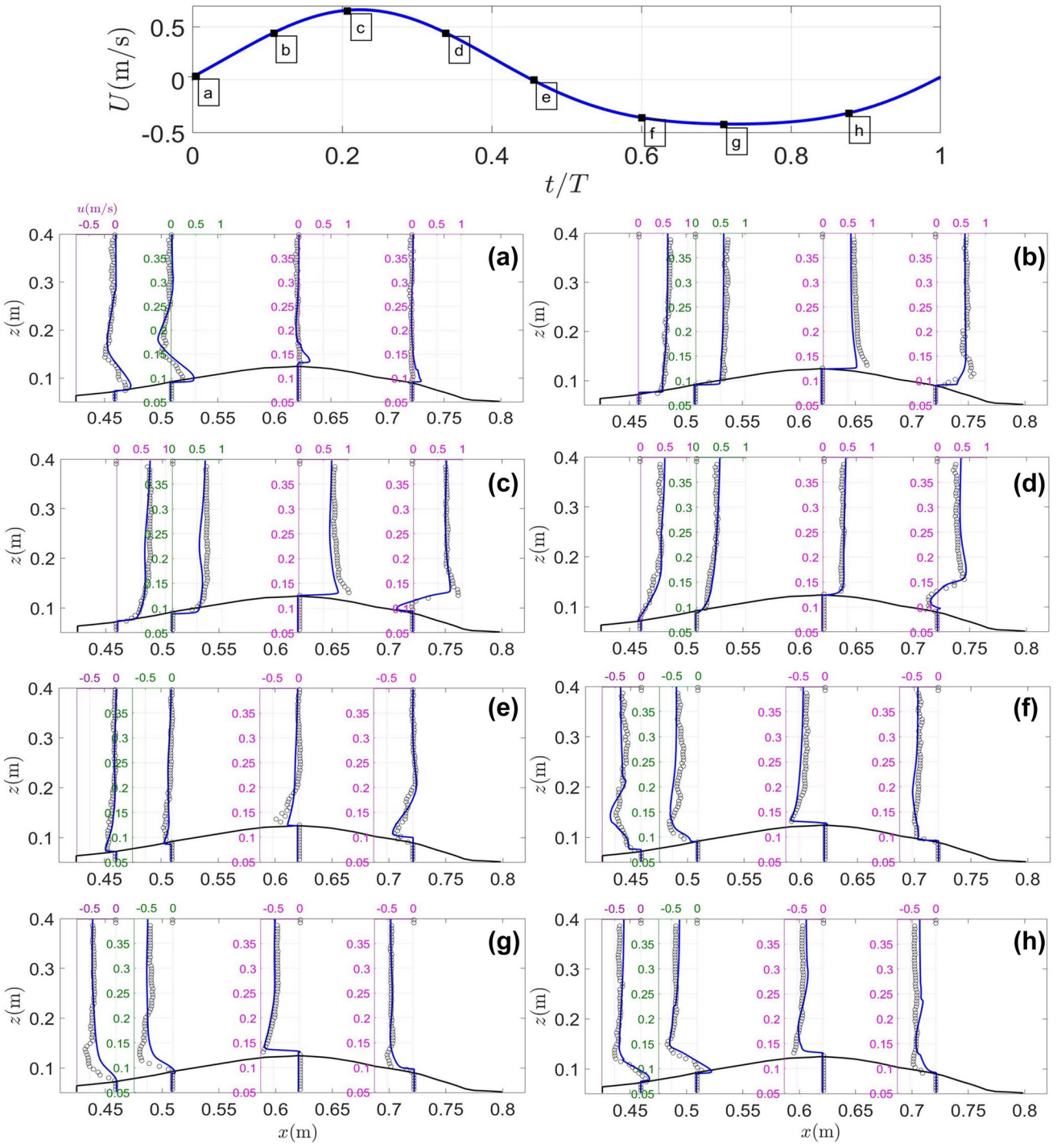

Figure 3. Comparison of the streamwise fluid velocity at eight different instances (panels (a)–(h)) between model results (solid curves) and measured data (symbols). Each panel shows velocity profiles at four locations over the ripple. The top panel presents the time-series of free-stream velocity with different instances shown in panels (a)–(h) indicated.

$x = 0.46$ and 0.51 m). These discrepancies may be due to the limitation of $k - \epsilon$ closure to accurately predict flow over bluff bodies, particularly, the flow separation and vortex shedding processes. As we will discuss in great detail later using the modeled vorticity, the vertical variation of velocity profiles shown here are due to complex vortices generation, ejection, and local flow acceleration over ripple and the numerical model can reproduce these key flow features with reasonable accuracy when compared with measured data.

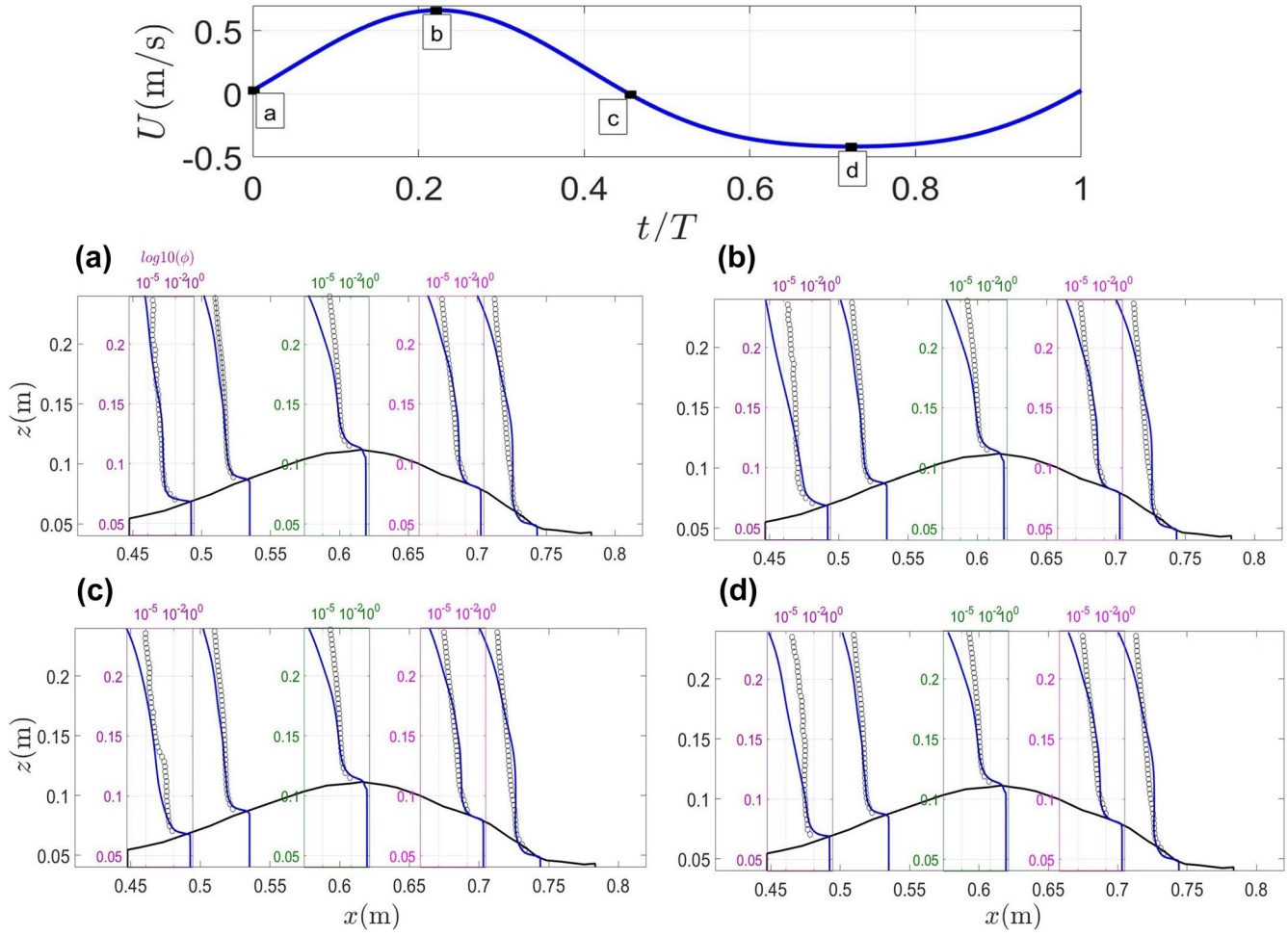

Figure 4. Comparison of sediment volumetric concentration at four different instances (panels (a)–(d)) between model results (solid curves) and measured data (symbols). Each panel shows concentration profiles at five locations over the ripple. The top panel presents the time-series of free-stream velocity with different instances shown in panels (a)–(d) indicated.

Meanwhile, sediment volumetric concentration profiles (see Figure 4, only four instances are shown for brevity) show good agreement with measured data within a distance about one ripple height above the ripple's surface throughout the entire wave cycle. In the dilute regions away from the ripple, however, the model underpredicts suspended sediment concentration. The underprediction generally occurs when sediment volumetric concentration is already below 10^{-3}. Since a strong turbulence-sediment interaction is expected due to the present coarse sand characteristics (Stokes number $St >> 1$, see Equation 12), using a more accurate turbulence-resolving approach (e.g., LES) may be necessary to better resolve turbulence-sediment interaction and predict the suspended sediment field. Also, the grain size is assumed to be uniform in the present Eulerian model while, in the experiment, some fine sands are present. This can explain some of the discrepancies between the model results and the measured data in the dilute region as the finer sands can stay suspended higher in the water column. The agreements between our modeled flow velocity and sediment concentration with measured data are similar to the earlier model studies (e.g., Chen & Yu, 2015). As we will entail next, complex vortex dynamics and sediment transport take place close to the ripple and a good agreement of in moderate to high concentration near the ripple is vital to further predict ripple migration rate.

To better illustrate the complex flow and sediment transport features over ripples, we investigate the vorticity dynamics along with the sediment fluxes. In the present 2DV study, the spanwise vorticity Ω is normalized by the oscillatory flow angular frequency ω as,

$$\Omega / \omega = \frac{1}{\omega}\left(\frac{\partial w^f}{\partial x} - \frac{\partial u^f}{\partial z}\right) \tag{21}$$

where u^f and w^f are horizontal and vertical velocity components, respectively. It is well-known that a significant amount of vorticity can be generated in the boundary layer region due to strong flow shear (velocity gradient), while the velocities magnitudes are small. Hence, identifying the vortex motion in the boundary layer region is challenging. Here, we follow the previous studies for flow over bedforms (Chen & Yu, 2015; Nichols & Foster, 2007), in which the modified swirling strength (Zhou et al., 1999) for vortex dynamics in the 2D oscillatory flow has been used and the normalized swirling strength is defined as,

$$\Lambda / \omega = \begin{cases} \frac{1}{\omega}\left(\sqrt{Q}\right) & Q \geq 0 \\ 0 & Q < 0 \end{cases} \tag{22}$$

where $Q = \left(\frac{\partial u^f}{\partial x}\frac{\partial w^f}{\partial z} - \frac{\partial u^f}{\partial z}\frac{\partial w^f}{\partial x}\right)$. The coherent structures are identified in the present study using $\Lambda / \omega = 1$. Finally, the sediment flux in the streamwise (x) direction $q = \phi u^s$ is presented also in its normalized form as

$$\Psi = \frac{q}{\sqrt{(s-1)gD_{50}^3}} \tag{23}$$

Although van der Werf et al. (2007) successfully measured the suspended sediment flux associated with the primary vortex ejection and shedding process, the near-bed sediment flux (sometimes referred to as bedload flux), which contributed to ripple migration, cannot be directly measured. Our goal is to fill a knowledge gap by elucidating a dynamic balance between sediment fluxes due to vortex formation near the ripple's surface and sediment avalanching on ripple flanks. Hence, Figure 5 is organized to simultaneously illustrate the temporal evolution of the modeled velocity and sediment concentration (left panels), normalized vorticity and swirling strength (middle panels), and sediment flux (right panels) at different instances for the middle ripple in Case 1. The top panel shows the free-stream velocity, which also signifies the eight phases (a–h) for different fields. For better visualization, only the flow and sediment fields between $z = 0.05 - 0.25$ m for the middle ripple are shown. The main characteristics of flow and sediment over the ripple bed are described as follows:

- During off-onshore flow reversal (Figure 5a), strong onshore-directed near-bed flow at the stoss side of the ripple can be seen (see velocity vectors in the left panel of Figure 5a). The near-bed flow leads the flow away from the bed, which is expected for the wave bottom boundary layer and local flow acceleration, or called speed-up (Charru & Franklin, 2012), due to the presence of ripple. At this moment, we observe two vortex structures on the stoss (offshore) side of the ripple flank (see middle panel of Figure 5a): the primary vortex, enclosed by the contour of $\Lambda / \omega = 1$ with positive (counterclockwise, red color) vorticity. This primary vortex is developed due to flow separation in the previous offshore flow (wave trough, see Figures 5g and 5h). Also, during its development, the primary vortex contributes to a thin onshore-directed boundary layer flow on the stoss flank which causes a region of negative vorticity (clockwise, blue color) near the ripple surface. Within this negative vorticity region in the vortex-induced boundary layer, we can also identify the secondary vortex (also enclosed by the contour of Λ / ω) attached to the ripple surface and underneath the primary vortex. This secondary vortex is the result of the adverse pressure gradient induced by the primary vortex and the ripple which yield to a secondary flow separation underneath the primary vortex itself. The existence of the secondary vortex has been revealed in direct numerical simulation studies by Blondeaux and Vittori (1991) and Önder and Yuan (2019). Indeed, the primary vortex appears to be forced away from the stoss flank by the clockwise secondary vortex (see middle panel of Figure 5b). Meanwhile, the clockwise secondary vortex on the stoss side is the nucleus of the primary clockwise vortex which is later formed on the lee (onshore) side of the ripple (follow Figures 5b and 5c). The vortex pair in the middle panel of Figure 5a

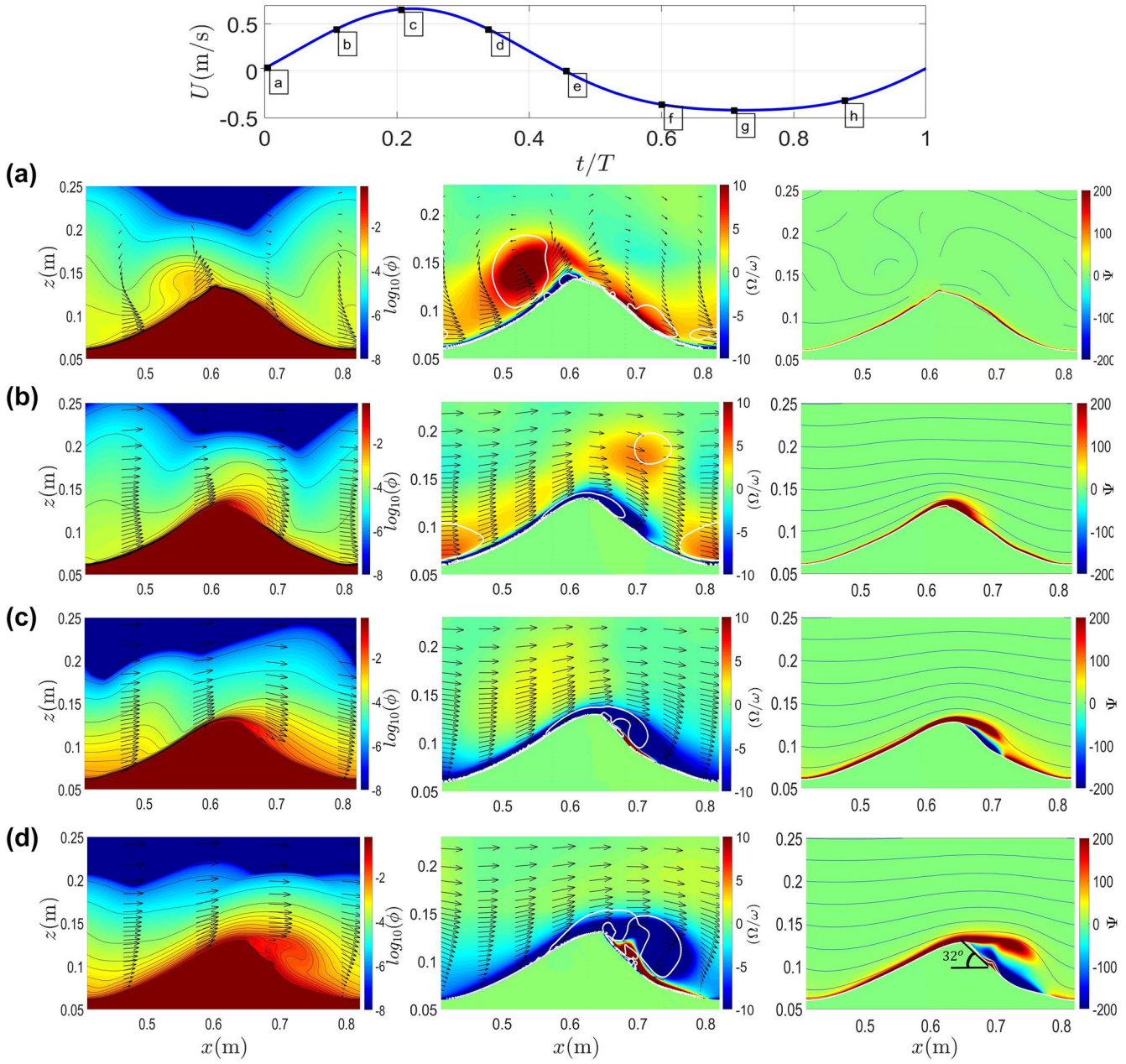

Figure 5. Snapshots of color contours of Case 1 for modeled sediment concentration field (left panels), normalized vorticity field and contour of swirling strength (white contour) (middle panels), and sediment horizontal flux (right panels) for eight instances (a)–(h) during a wave period. In each panel, the velocity field is downsampled and represented by the vectors. The blue lines in the right panels represent the flow streamlines. The top panel shows the time-series of free-stream velocity and the corresponding eight instances are indicated.

on the stoss flank produces a near-surface jet directed toward the ripple crest. In this so-called ejection stage, the strong flow carries the vortices toward the ripple crest while the strength of the primary vortex is reducing. The cloud of the sediment on the stoss side and the crest of the ripple (see left panel of Figure 5a) is associated with the vortex pair and are carried onshore. The horizontal sediment flux at this moment (see right panel of Figure 5a) is clearly onshore directed but mainly occurs very close to the bed.

- During the onshore flow acceleration shown in Figure 5b, flow separation and the generation of the primary vortex at the lee (onshore) side of the ripple becomes evident while the flow on the stoss

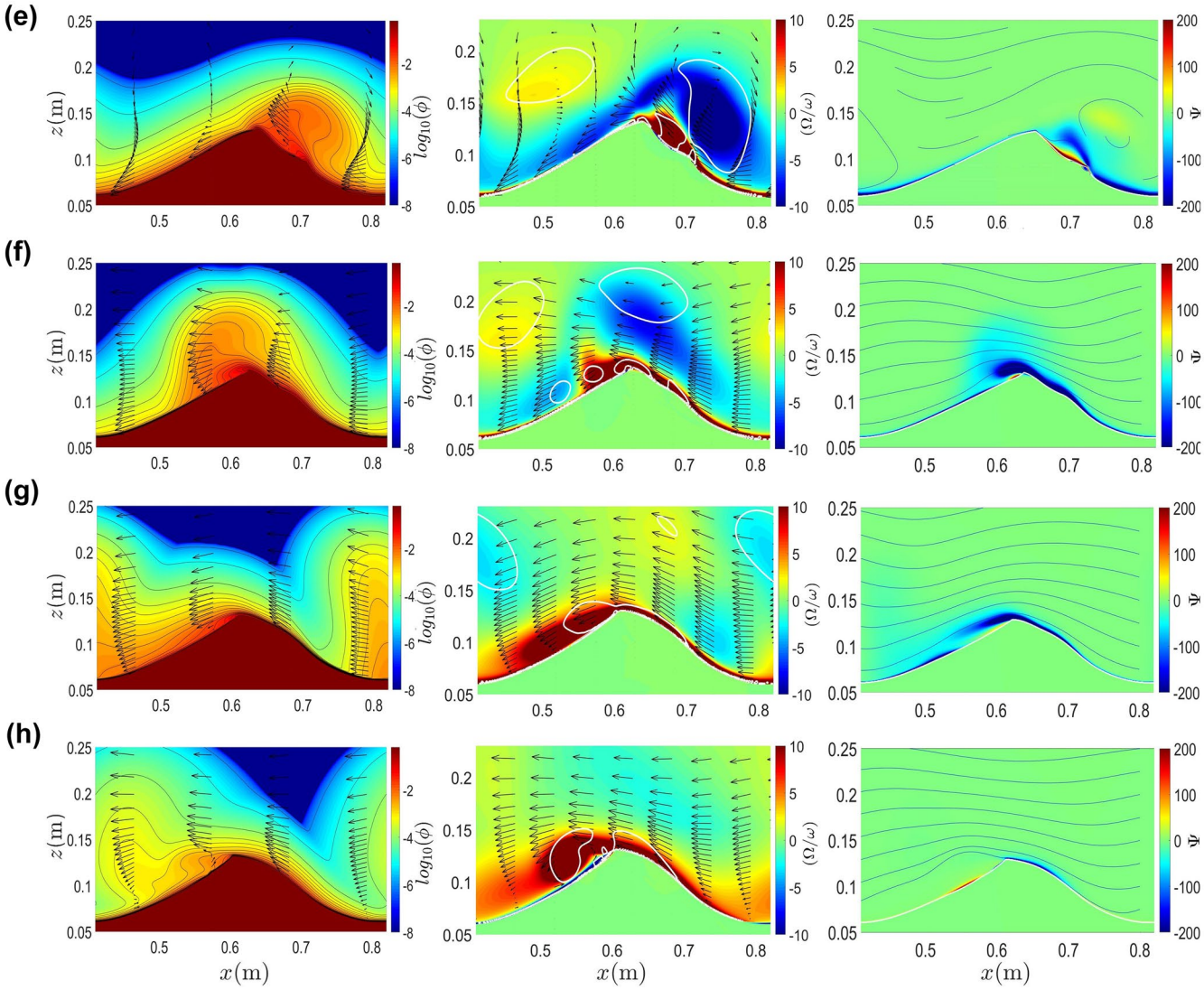

Figure 5. Continued.

(offshore) flank and around the crest continues to accelerate (see middle panel of Figure 5b). At this time, the primary vortex previously generated at the stoss side has passed over the ripple crest (now located at about $x = 0.72$ m and $z = 0.17$ m) while its intensity is reduced significantly. Meanwhile, the negative vorticity near the stoss side ripple surface and over the ripple crest is continuously fed onto the lee (onshore) side ripple flank. In the right panel of Figure 5b, we observe intense onshore-directed sediment transport with high sediment flux that occurs close to the ripple crest. Indeed, the attached boundary layer flow covering the stoss flank erodes sediments from the stoss flank which induces the intense near-bed sediment flux. This flux feeds the cloud of sediment trapped in the growing primary vortex on the lee (onshore) side of the ripple.

- During onshore peak flow (Figure 5c), flow separation at the lee (onshore) side of the ripple has expanded with more intense negative vorticity (middle panel). Over the lee (onshore) ripple flank, the primary vortex-induced (returning) boundary layer flow with a region of positive (counter-clockwise, red color) vorticity starts to emerge near the ripple's surface. Because the flow very close to the bed starts to be directed toward the ripple crest, besides the onshore (positive) sediment flux coming from the stoss side passing over the ripple crest, there is an offshore-directed sediment flux located very close to the bed (right panel). Also, the near-bed positive flux induced by the boundary layer flow on the stoss

flank is more intense than the one produced by the offshore flow peak boundary layer flow (compare right panel in Figures 5c and 5g).

- During onshore flow deceleration (Figure 5d), the clockwise primary vortex (the negative vorticity region enclosed by the contour of $\Lambda / \boldsymbol{\omega}$) on the lee (onshore) side of the ripple has reached its maximum strength (middle panel). Meanwhile, a cloud of sediment trapped in the primary vortex can be seen (left panel in Figure 5d). The secondary counterclockwise vortex underneath the primary vortex on the lee (onshore) side has emerged clearly (see the positive vorticity region near the ripple's surface) within the (returning) boundary layer flow induced by the primary vortex. While some of the sediments continue to be swept over the crest toward the onshore direction by the primary vortex, a significant amount of sediment stays close to the bed and is directed offshore by near-bed flow associated with the vortex-induced (returning) boundary layer flow (right panel). Interestingly, due to the steep slope at the lee (onshore) side of the ripple near the crest, some sediments are observed to avalanche down the slope, causing a small onshore directed flux very near the ripple's surface at around $x = 0.65$–0.7 m (right panel). It is worth noting that in the present model, avalanching occurs naturally when the downslope gravitational force exceeds upslope force and there is no need to include an artificial avalanching scheme (e.g., Marieu et al., 2008). The resolved avalanching process maintains the slope of the lee-side ripple to be about 32°.
- At the time of on-offshore flow reversal (Figure 5e), the primary vortex (with negative vorticity) on the lee (onshore) side of the ripple is lifted and start to be ejected by the secondary vortex (with positive vorticity) underneath it. This vortex pair is evidently stronger than that appeared during off-onshore reversal (compare the middle panel of Figures 5e and 5a) and causes a more intense offshore jet right above the ripple crest. This jet moves the primary vortex toward the ripple crest and a significant amount of sediment is suspended over the lee (onshore) ripple flank (see left panel of Figure 5e), which will be carried offshore during the wave trough period (negative velocity interval). Sediment flux carried by the primary vortex has all become offshore directed (see right panel) while close to the ripple crest and over the lee (onshore) ripple flank, a positive (onshore-directed) sediment flux due to avalanching still exists. While it has been shown in laboratory observations, for instance, by van der Werf et al. (2007), that a significant amount of offshore sediment transport by suspended load occurs during on-offshore flow reversal via ejection, the present model results further demonstrate the role of near-bed avalanching in reducing total offshore transport flux and hence contribute to onshore ripple migration.
- During offshore flow acceleration (Figure 5f), a large cloud of the sediment above the ripple crest carried by the primary vortex ejected from the lee (onshore) side of the ripple (left panel) can be clearly seen and its considerably large size can be contrasted with that during onshore flow acceleration (see left panel of Figure 5b). Concurrent to the passage of the primary (clockwise) vortex now located much higher above the ripple crest moving offshore, the secondary counterclockwise vortex previously generated on the lee (onshore) side ripple flank is now stretched beyond the ripple crest over the stoss (offshore) side of the ripple which will soon form the primary vortex during offshore flow (see the middle panel in Figures 5g and 5h). At this moment, offshore directed sediment flux prevails almost throughout the entire ripple.
- During offshore peak flow (Figure 5g) and offshore flow deceleration (Figure 5h), the flow patterns are similar to those shown in Figures 5c and 5d during onshore flow, but the flow intensity on the stoss (offshore) side of the ripple is much weaker due to onshore velocity skewness of the free-stream flow. Consequently, the flux on the lee flank due to boundary layer flow is weaker than the one on the stoss flank during the onshore deceleration phase. The complexity of the sediment flux on the stoss (offshore) side of the ripple is less obvious because the vortex generation and ejection process are weaker. From the sediment flux shown in the right panels, avalanching almost does not occur because the slope on the stoss (offshore) side of the ripple is milder.

In summary, the velocity intensity near the rippled bed is larger than free-stream velocity due to the presence of the ripple causing local flow acceleration (speed up) toward the ripple crest and leading to vortex ejection (Figures 5a–5c). This onshore accelerating flow is also fueled by the return flow of the stoss primary vortex. Meanwhile, flow reversal near the bed occurs earlier than free-stream reversal due to the wave bottom boundary layer phase lead. During the onshore half cycle, the stoss (offshore) ripple flank mainly

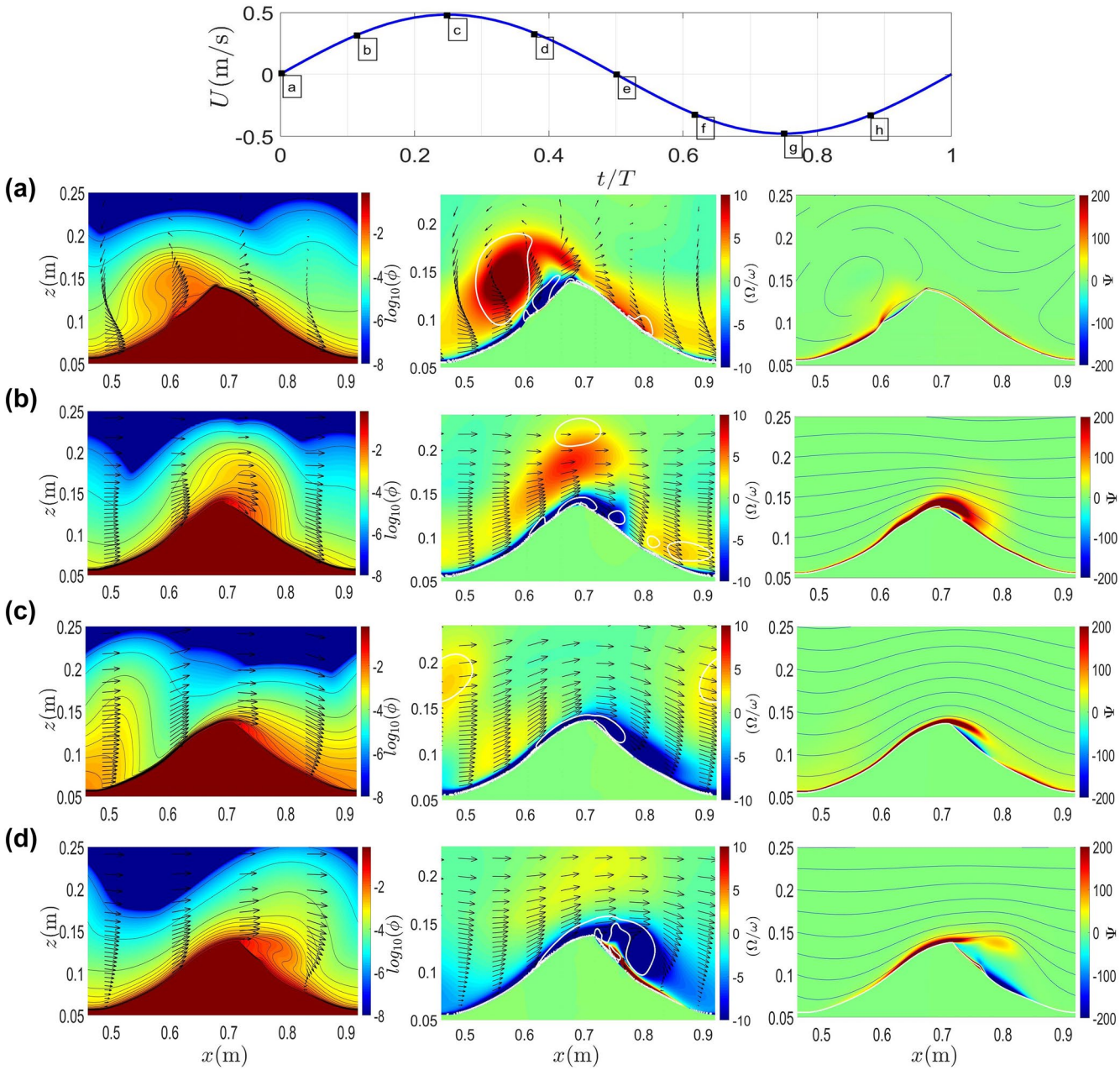

Figure 6. Snapshots of color contours of Case 2 for modeled sediment concentration field (left panels), normalized vorticity field and contour of swirling strength (white contour) (middle panels), and sediment horizontal flux (right panels) for eight instances (a)–(h) during a wave period. In each panel, the velocity field is downsampled and represented by the vectors. The blue lines in the right panels represent the flow streamlines. The top panel shows the time-series of free-stream velocity and the corresponding eight instances are indicated.

experiences onshore sediment flux, which occurs very close to the ripple's surface, while the suspended sediment flux that occurs away from the ripple is negligible (Figure 5b). As the onshore phase proceeds, the near-bed sediment flux on the stoss flank continues to feed the cloud of sediment trapped in the growing lee (onshore) side primary vortex where a considerable amount of the sediment is suspended. Meanwhile, the remaining of the sediments that stayed close to the ripple bed are carried offshore toward the ripple crest by primary vortex-induced boundary layer (returning) flow (Figure 5c). High shear driven by the returning boundary layer flow along with the secondary vortex may also erode and transport some resuspended sediments from the lee (onshore) ripple flank toward the crest. However, this offshore transport flux is limited

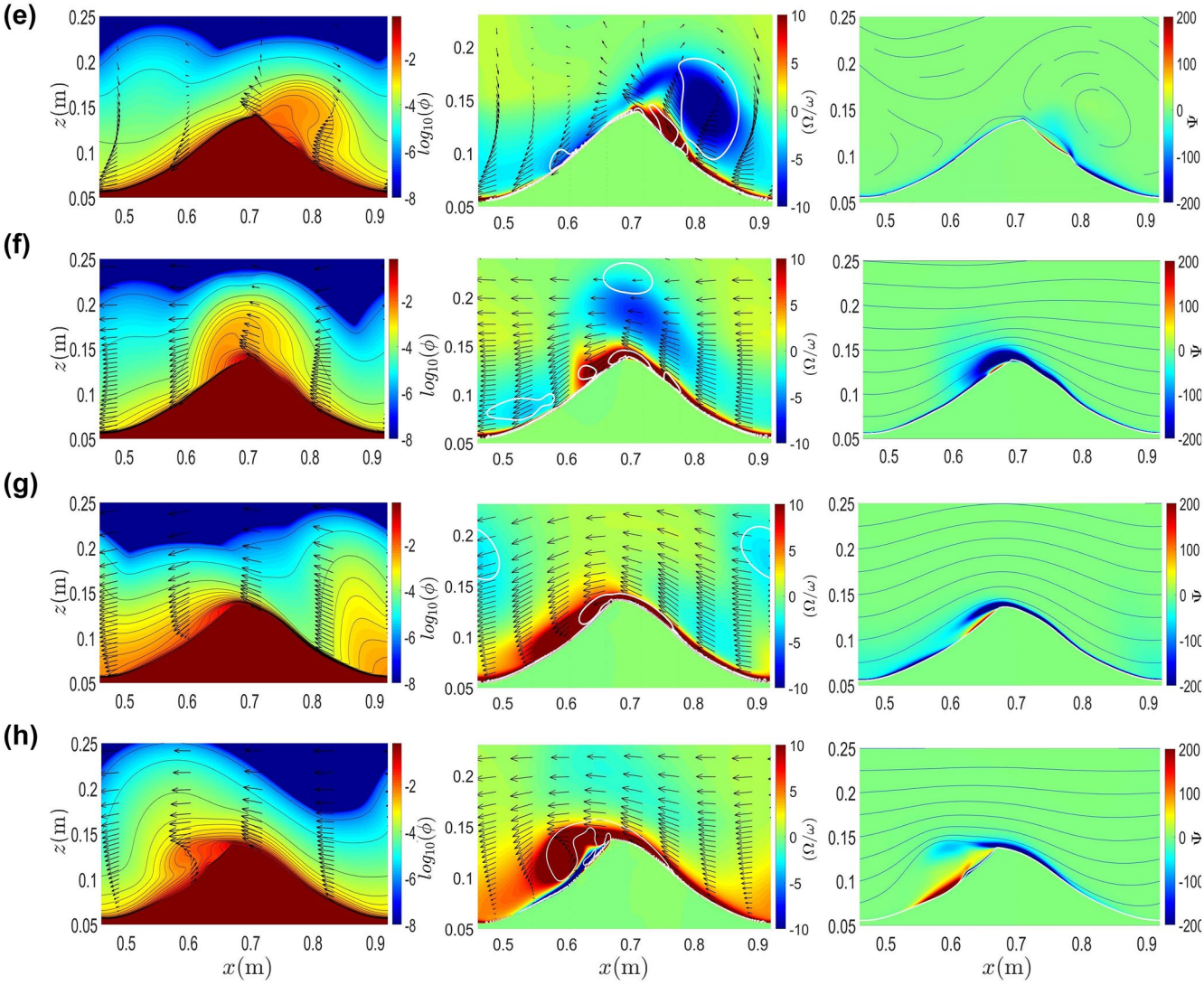

Figure 6. Continued.

by sediment avalanches down the slope when the slope of the ripple flank becomes greater than the angle of the repose (see Figure 5d). During the on-offshore flow reversal and early offshore half cycle, a large amount of suspended sediment trapped in the lee (onshore) side primary vortex is advected offshore and meanwhile, the ejection also drives a significant offshore-directed near-bed sediment flux which starts to feed the cloud of the sediment over the stoss (onshore) ripple flank (Figures 5e and 5f). This process, although much weaker than the onshore cycle, continues to feed sediment in the offshore side of the ripple (Figures 5g and 5h) before the next ejection occurs (Figure 5a).

The onshore-directed velocity skewness of the free-stream velocity in Case 1 causes asymmetric vortex formation-ejection on ripple flanks and leading to an imbalance between offshore/onshore suspended sediment flux (mainly due to primary vortex generation and shedding) and near-bed sediment flux (mainly due to primary vortex-enhanced boundary layer flow acceleration over the ripple and sediment avalanching) over one wave period. The imbalance between suspended fluxes produces an offshore directed net flux above the ripple crest, which has already been documented by many earlier studies (e.g., van der Werf, 2007). The present model results do not only confirm this finding but also reveal the significance of net onshore-directed near-bed sediment flux in response to the onshore-directed velocity skewness.

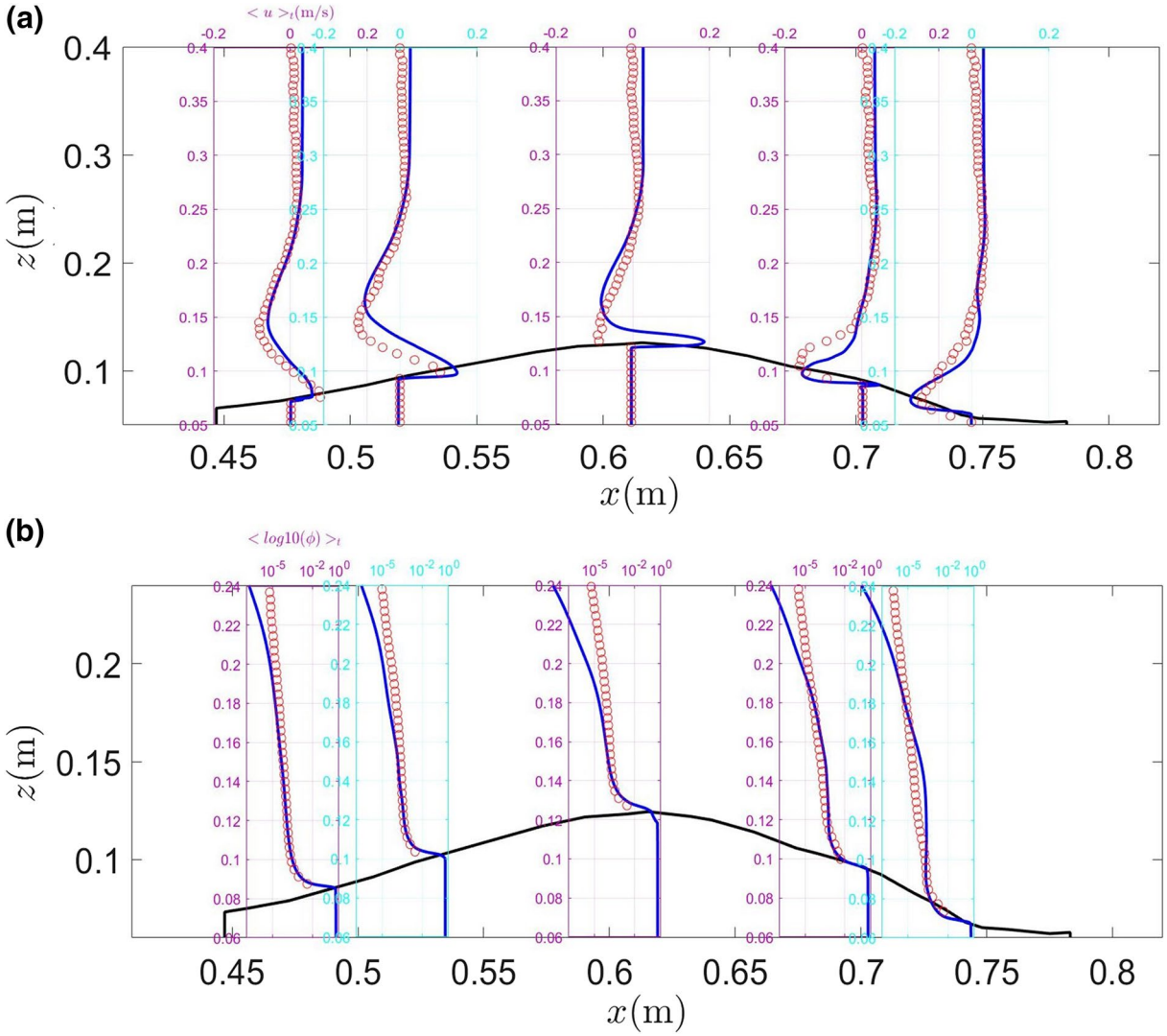

Figure 7. A comparison of wave-period-averaged (a) flow velocity profiles and (b) sediment volumetric concentration profile above the ripple at five different locations between model results (line) and measured data (symbol) reported by van der Werf et al. (2007).

In contrast, in Case 2 of sinusoidal (symmetric) free-stream flow, velocities, sediment concentration, the vortex formation-ejection process, and horizontal sediment fluxes show completely symmetric behavior on the lee (onshore) flank (during the onshore half cycle) and stoss (offshore) flank (during the offshore half cycle) of the ripple, see Figure 6. For instance, the primary vortex ejected from the opposite side of the ripple, the primary vortex-induce returning flow near the ripple's surface, and the growing secondary vortex at the off-onshore and on-offshore flow reversals are exactly the same (in size and strength) but with different vorticity signs (compare the middle panel of Figures 6a and 6e). Therefore, suspended sediment fluxes due to symmetric generation and shedding of primary vortices cancel each other out. Similarly, the sediment fluxes driven by the flow near the ripple's surface, vortices, and sediment avalanching are also symmetric with different signs. For instance, during onshore flow deceleration (right panels of Figures 6c and 6d) there is an onshore near-bed sediment flux originated from the stoss (offshore) side which supplies sediment to the lee (onshore) side primary vortex. Also, very close to the ripple's surface on the lee (onshore) ripple flank, there is an offshore sediment flux generated by the primary vortex-induced returning boundary layer flow along with a small onshore flux produced by the sediment avalanching close to the ripple crest (right panel of Figure 6d). The same flow structure and flux magnitude but with different signs can be found during the offshore deceleration phase (Figures 6g and 6h). Essentially, due to this behavior, the ripple's shape

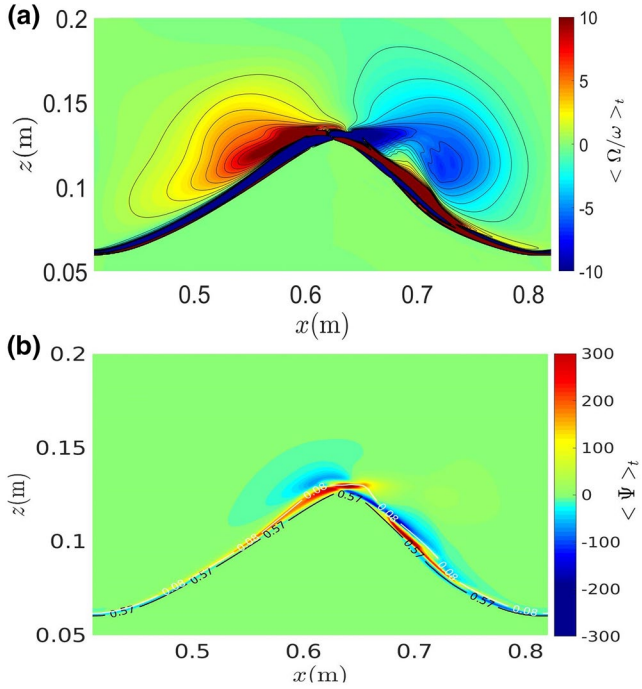

Figure 8. (a) Wave-period-averaged normalized vorticity (color-bar) for Case 1. Panel (b) shows the corresponding wave-period-averaged normalized sediment horizontal flux, and the black and white contours represent the sediment volumetric concentration of $\phi = 0.57$ and $\phi = 0.08$, respectively.

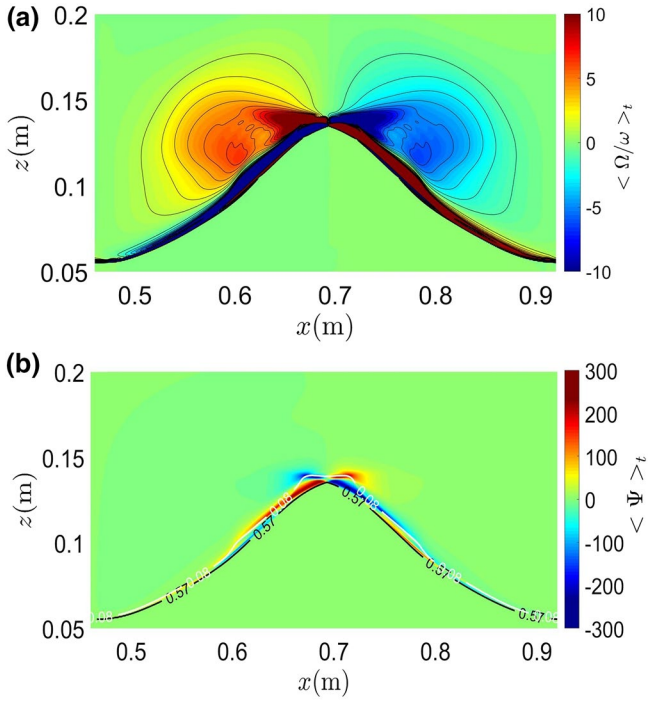

Figure 9. (a) Wave-period-averaged normalized vorticity (color-bar) for Case 2. Panel (b) shows the corresponding wave-period-averaged normalized sediment horizontal flux, and the black and white contours represent the sediment volumetric concentration of $\phi = 0.57$ and $\phi = 0.08$, respectively.

is symmetric about the ripple crest, and the ripple migration and total net transport rate are zero. A more quantitative analysis of migration and net transport will be presented in the next section.

4.3. Averaged Flow

Since sediment transport over ripple is the result of a small imbalance between the intrawave variation, we further validate the model using wave-period (time) averaged velocity profiles and sediment volumetric concentration at five different locations above the middle ripple (Figures 7a and 7b) for Case 1. The time-averaged velocity profiles are asymmetric between the lee (onshore) side and the stoss (offshore) side of the ripple due to the asymmetric vortex generation (Figure 7a). Modeled time-averaged velocities show fair agreement with the measured data. Due to onshore velocity skewed free-stream velocity, both the measured data and model results indicate an intense, offshore directed flow close to the onshore side of the ripple's surface and ripple crest, which is the signature of stronger vortices during onshore flow and hence more intense ejection around on-offshore flow reversal. However, there are also some differences between measured and model velocity profiles. Very close to the ripple's surface at the ripple crest, model results show a positive time-averaged flow while the experimental data shows negative mean flow all the way to the ripple's surface. The onshore near-bed mean flow velocity at the ripple crest predicted by the model is consistent with the larger flow intensity during the crest period (positive velocities) which leads to more significant flow speed-up (Charru & Franklin, 2012) and hence larger onshore transport via near-bed load (see right panels of Figures 5c and 5d). This onshore flow at ripple crest has only a thickness of about 1 cm and it is likely that this feature cannot be resolved by PIV measurement in such a high concentration region near the bed. Modeled time-averaged volumetric sediment concentration profiles show very good agreement with the experimental data except in the dilute region far away from the ripple (see Figure 7b) where sediment concentration is underpredicted by the model. This feature is consistent with the time-dependent sediment volumetric concentration shown in Figure 4. Overall, the computed correlation coefficient (R^2, or coefficient of determination) and the root-mean-square error (E) between the model results and the experimental data are $R^2 = 0.8929, E = 0.0083$ for averaged velocity field, and $R^2 = 0.8652, E = 0.0071$ for sediment volumetric concentration field, indicating a good agreement between the model results and the measured data.

Driven by periodic wave motions, wave-period-averaged sediment horizontal flux can be decomposed into the flux of wave-period-averaged flow and averaged intrawave flux (e.g., Nielsen, 1986). Our analysis of the present model results suggests that the relative magnitudes of these two components are complex and both components are important to the total flux. However, as mentioned before, the vortex formation-ejection process shown in Figures 5 and 6 controls the flow field above the ripple bed which dynamically shapes the ripple geometry and forces the ripple migration. Our model results indicate that wave-period-averaged sediment horizontal flux and wave-period-averaged vorticity are highly correlated. The wave-period-averaged normalized vorticity field for Case 1 (Figure 8a) shows a larger primary vortex at the onshore side of the rip-

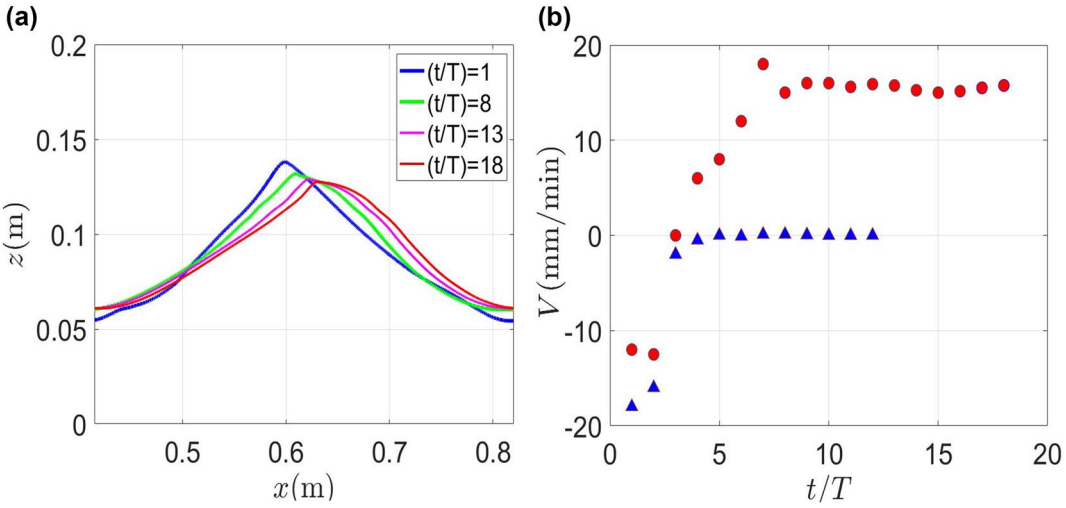

Figure 10. (a) Ripple profile for the middle ripple in Case 1 at different wave cycle visualized using the contour of volumetric concentration $\phi = 0.57$. (b) Ripple migration rate as a function of the number of wave's cycle for the middle ripple in Case 1 driven by onshore velocity skewed oscillatory flow (red circles) and Case 2 driven by sinusoidal oscillatory flow (blue triangles).

ple (negative/clockwise vorticity), reflecting the stronger onshore flow driven by onshore velocity-skewed wave motion. Below the primary vortex, the strip of vorticity at the onshore side of the ripple (positive/counterclockwise vorticity) is limited by sediment avalanching causing some negative vorticity very close to the ripple's surface. The size of this strip of vorticity is smaller than the one on the offshore side of the ripple (negative/clockwise vorticity). Consequently, wave-period-averaged normalized sediment flux for Case 1 (Figure 8b) is also asymmetric. There is a notable offshore-directed sediment horizontal flux occurring at about 1 cm above the ripple's surface near the ripple crest and the offshore side of the ripple with sediment lower than $\phi = 0.08$. This is caused by the more significant vortex pair and strong on-offshore ejection associated with the passage of wave crest. The near-bed sediment horizontal flux between the contour of $\phi = 0.08$ and $\phi = 0.57$ is also asymmetric but shows a larger and more extensive onshore directed sediment flux. This pronounced net onshore-directed near-bed flux due to onshore velocity skewness and sediment avalanching is what forces the asymmetric ripple geometry and onshore ripple migration. On the other hand, in Case 2 (Figure 9a) with sinusoidal (symmetric) oscillatory motion, the primary vortices and the near-bed strips of vorticity are symmetric about the ripple crest but with clockwise and counterclockwise rotation. The sediment horizontal fluxes above and below the contour of $\phi = 0.08$ as well as at the onshore side or offshore side of the ripple are both symmetric and hence they cancel each other out. The resulting net transport rate and ripple migration rate are zero.

Figure 10a shows the ripple profiles for the middle ripple in Case 1 at the selected wave cycle using the contour of volumetric concentration $\phi = 0.57$. It can be seen that from the start of the simulation, the ripple adjusts its shape and reduces its height, and more importantly migrate slowly to the onshore direction. By tracking the ripple crest based on the ripple profile shown in Figure 10a for each wave cycle, the resulting onshore ripple migration rate is estimated in Figure 10b (see circles). After the first eight wave periods, the migration rate reaches an equilibrium value of around $V = 15$–16 mm/min, which is very close to the observed migration rate of 18 mm/min reported by van der Werf (2007). We also calculate the ripple migration rate by tracking the ripple trough. This procedure is conducted for Case 1 and the modeled ripple migration rate is $V = 14$–15 mm/min, which is just slightly smaller than the migration rate obtained by tracking the ripple crest. The modeled onshore ripple migration is consistent with the dominant onshore sediment flux that occurs very near the ripple's surface discussed in Figures 5 and 8. Following Nielsen (1992), by assuming zero near-bed transport rate at the ripple trough, the net near-bed transport rate (Q_{mig}) is related to the ripple migration speed as,

$$Q_{mig} = f\phi_{bed}V \tag{24}$$

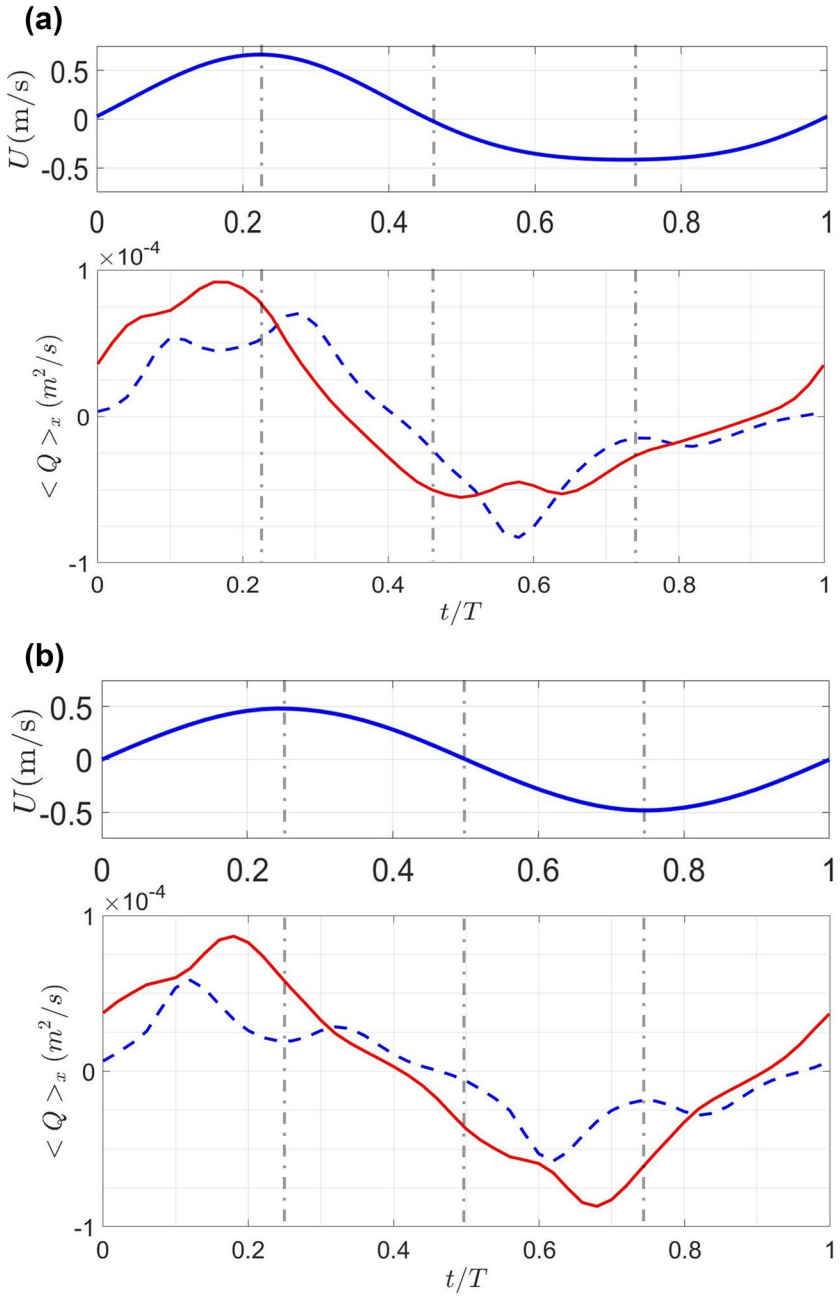

Figure 11. Time series near-bed load transport (solid red line) and suspended load (blue dash-line) and for (a) Case 1 and (b) Case 2. The top panel in each figure shows the free-stream velocity time-series. The dash-dot-lines are showing the timing of the flow peaks and the reversal.

where $f = 0.5$ is the shape factor by assuming an idealized triangular bedforms and), $\phi_{bed} \approx 0.6$ is the ripple bed volumetric concentration and $\eta = 0.075m$ is the simulated equilibrium ripple height. By substituting the simulated near-bed transport rate of $Q_{\text{bm}} = 4.5 \times 10^{-6}$ m^2/s (see more discussion later) into Equation 24, the calculated migration rate is $V = 12$ mm/min. The small discrepancy between the simulated migration rate and the calculated migration rate using Equation 24 is due to the ideal triangular bedform assumption (or if we use a shape factor 0.4, we obtain the same migration speed with the simulated results). A similar analysis is carried out for Case 2 and the resulting migration rate is confirmed to be zero (see Figure 10b,

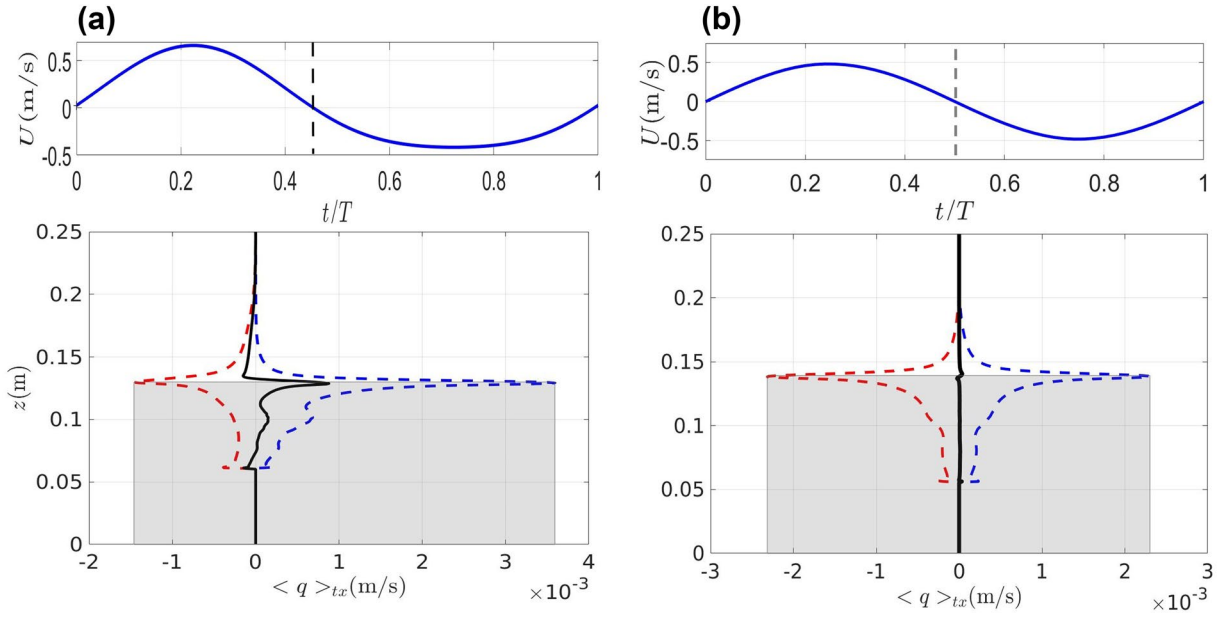

Figure 12. Streamwise (ripple)-averaged and time-averaged sediment flux profile for onshore flow interval (blue dash-line), offshore flow interval (red dash-line), and the entire wave period (black solid-line) for Case 1 (panel a) and Case 2 (panel b). The top panels show the free-stream velocity for each case in which the positive and negative velocities are separated by the gray dash-line. The gray region in panel (a) and (b) shows the near-bed load region (the region below z_{s0}).

triangles). We like to reiterate that the calculated ripple migration speed is insensitive to the small change of critical concentration used to identify the ripple bed profile.

To better quantify the onshore transport via ripple migration (near-bed load transport) and offshore transport via suspended load transport, the time series of horizontally (x-) averaged sediment transport rate (i.e., sediment transport rate averaged over one ripple length for the middle ripple) is presented in Figure 11. To facilitate the distinction between suspended load and near-bed load, we partition transport flux into two regions using the two grain diameter above the mean location of ripple crest $z_{s0} = z(crest) + 2D_{50}$ as demarcation. This definition of z_{s0} is consistent with literature where the bottom boundary of the suspended load model over ripple bed is defined (Nielsen, 1986). Then, the near-bed load transport rate Q_b is calculated by integrating (with respect to the vertical direction) the sediment flux from the bottom of the domain to two grain diameter above the ripple crest:

$$Q_b = \int_{z=0}^{z=z_{s0}} q(z)\,dz \tag{25}$$

The suspended load transport rate Q_s is then defined as transport above $z = z_{s0}$ to the top of the model domain:

$$Q_s = \int_{z=z_{s0}}^{z=L_z} q(z)\,dz \tag{26}$$

The time series of horizontally (x)-averaged transport rates for Case 1 and Case 2 over one period are shown in Figures 11a and 11b, respectively. During the onshore flow acceleration period, near-bed load transport is the dominant component until just passing the onshore peak flow. During the subsequent onshore flow deceleration phase, the primary vortex is sufficiently large to trap and transport a considerable amount of suspended load and the near-bed load is of less importance. During offshore flow acceleration and approaching the time of offshore flow peak, the suspended load is again dominant which is due to stronger ejection of vortex pair from the lee (onshore) side of the ripple. Clearly, in Case 1 with onshore velocity skewed wave motion, near-bed load transport is dominant during the onshore flow phase (wave crest),

leading to onshore transport, while suspended load becomes dominant during offshore flow (wave trough), leading to offshore transport. For comparison, in Case 2 with symmetrical sinusoidal wave motion, both near-bed load transport and suspended load transport are symmetric in onshore and offshore phases and leading to zero net transport rate and ripple migration (Figure 12b). However, it is interesting to point out that unlike the migrating Case 1, in the complete equilibrium condition (equilibrium in both ripple geometry and migration) of Case 2, the near-bed load is dominant over the suspended load almost throughout the entire wave cycle. This implies the importance of suspended load driving sediment transport when ripples are out-of-equilibrium.

In Figure 12, the time- and ripple-averaged sediment flux profiles are plotted for Case 1 (panel a) and Case 2 (panel b), in which the shaded region shows the area below z_{s0} (near-bed load region). To illustrate the asymmetry of sediment fluxes in Case 1, time-averaging is carried out and presented for only the onshore flow interval (wave crest, blue dash-line) and the offshore flow interval (wave trough, red dash-line). Sediment flux is mostly onshore directed during onshore flow intervals (see the blue dash-line in Figure 12a), and the majority of sediment flux is confined between the ripple crest and trough, consistent with the near-bed load dominance discussed before. More importantly, the peak onshore flux with very high intensity occurs at the ripple crest, as shown in Figure 5. During the offshore flow interval (red dash-line in Figure 12a), the flux is offshore directed and it stretches much higher in the water column due to stronger vortices generation in the lee (onshore) side of the ripple and subsequent ejection to the offshore direction. Evidently, the suspended load flux in the offshore flow interval is much more important than that during the onshore flow interval.

When taking time-average over the entire wave period (see the black solid-line in Figure 12a), the model result shows an offshore-directed (negative) sediment flux above z_{s0} due to suspended load while below z_{s0}, near-bed sediment flux is mostly onshore-directed (positive). Again, the peak onshore sediment flux occurs at the ripple crest level around $z = 0.125$ m (see the blue-dashed curve in Figure 12a), consistent with the large onshore flux around the ripple crest shown in Figure 8b. The complex sediment flux structure, manifested here as a zig-zag feature in the vertical profile, is due to various sediment fluxes, such as the near-bed flux driven by wave asymmetry, vortex ejection, and avalanching discussed in Figures 5 and 8.

By integrating the flux below z_{s0} (shaded region), the net near-bed load sediment transport rate predicted by the model is $Q_{bm} = 4.5\times10^{-6}$ m^2/s (onshore), which is coincidentally identical to the measured value of $Q_{be} = 4.5\times10^{-6}$ m^2/s estimated based on the ripple migration rate by van der Werf et al. (2007). The onshore near-bed sediment flux due to the sediment avalanching (positive flux on the lee flank between the contour of $\phi = 0.57$ and $\phi = 0.08$ in Figure 8b) is calculated as $Q_{ava} = 1.485\times10^{-6}$ m^2/s which is 33% of the total onshore near-bed transport rate. However, the modeled net suspended transport rate, integrated from z_{s0} to the top boundary, is $Q_{sm} = -4.2\times10^{-6}$ m^2/s which is approximately half of the measured value ($Q_{se} = -8.2\times10^{-6}$ m^2/s). This difference between the measured and modeled suspended load transport may be related to the turbulence closure that is used in the model and the underprediction of the vortex intensity at the lee side of the ripple during the onshore flow. Consequently, the total net sediment transport rate is very small $Q_{tm} = 0.3\times10^{-6}$ m^2/s in the model while the measured total net sediment transport rate using sediment traps is offshore directed ($Q_{te} = -3.7\times10^{-6}$ m^2/s). Our numerical model results are consistent with those obtained by the more complex high-fidelity LES-DEM approach of Finn et al. (2016) in which they also modeled onshore ripple migration ($V = 14$ mm/min) while the net sediment transport rate was onshore directed ($Q_t = 8.7\times10^{-6}$ m^2/s).

Accordingly, the sediment flux profiles for Case 2 are shown in Figure 12b. Since we observe a completely symmetric behavior about the flow reversal in Figure 6, the onshore sediment flux profile averaged under wave crest interval (blue dashed line) is of the same magnitude, but in opposite direction, as compared to the offshore sediment flux profile averaged under the wave trough interval (red dashed line). As a result, the time-averaged sediment flux over the entire wave period in Case 2 is zero (see the black solid line in Figure 12b).

5. Conclusion

In this study, an Eulerian two-phase model for sediment transport, SedFoam has been applied to simulate sediment transport and migration of orbital ripple driven by onshore velocity-skewed (second order Stokes) and symmetric (sinusoidal) oscillatory flows, both of which are similar to the oscillating tunnel experiments conducted by van der Werf et al. (2007). The model results show good agreement with measured data for ripple shapes and dimensions. The time-dependent and time-averaged intrawave fluid velocity and sediment concentration fields, when compared with the measured data for the onshore velocity-skewed case, also show a reasonably good agreement with measured data. The model underpredicts suspended sediment concentration in the dilute region away from the ripples, which contribute to the underprediction of offshore sediment flux in suspended load. However, the model is able to predict the onshore ripple migration rate that agrees well with measured data, consistent with the good agreement in the modeled sediment concentration and flow velocity near the ripple's surface.

Besides the primary vortex generation-ejection process, which is particularly important for simulating suspended sediment flux, the model is able to capture accelerating boundary layer structure near the ripple's surface which is further enhanced by the returning flow of the primary vortex, and the secondary vortex generation-ejection similar to previous clear fluid DNS results. Our numerical investigation further reveals its significance for modeling of near-bed sediment flux very close to the ripple's surface. The model shows that the secondary vortex generated on a ripple flank is the nucleus of the primary vortex generated on the other side of the ripple. In the case of the symmetric forcing, the generation of the vortices is symmetric about the ripple crest, while in the case of velocity-skewed flow, it is asymmetric and leading to net sediment transport and ripple migration.

The model results confirm that the ripple shape is controlled by the vortex generation which depends on the flow velocity skewness. Due to the symmetric behavior of vortices above the ripple in sinusoidal oscillatory flow, the final modeled ripple shape is symmetric about the ripple crest. However, in the onshore velocity-skewed oscillatory flow, the modeled ripple has a steeper flank on the lee side (onshore side) compared to that of the stoss (offshore) side, due to asymmetric near-bed sediment flux and avalanching of sediment on each flank.

Without conventional bedload/suspended load assumption embedded in the present model design, model results are used to reveal the contribution from near-bed load transport and suspended load transport over ripples in oscillatory flow. In the case of onshore velocity skewed oscillatory flow, both near-bed load and suspended load fluxes are asymmetric. In the onshore half cycle, the near-bed load is onshore directed while the suspended load is of minor importance. In the offshore half cycle, both fluxes are offshore directed, and the suspended flux is dominant. Hence, similar to the experimental data (e.g., van der Werf et al., 2007), the model results indicate an offshore directed net suspended sediment flux consistent with the generation of a larger and stronger vortex pair on the lee (onshore) side of the ripple under onshore velocity skewed oscillatory flow. Model results also reveal that the net near-bed flux is onshore directed, which forces the onshore ripple migration due to asymmetric boundary layer flows near the ripple surface and sediment avalanching. This near-bed sediment flux and the resulting ripple migration cannot be directly resolved or measured in the previous study.

As it is shown in the model results, the suspended sediment volumetric concentration above the ripple in the dilute region was underpredicted by the present model. We suspect this discrepancy is related to the limitation of k-ε turbulence closure used in the present model. Future work is needed to critically evaluate turbulence closure in the turbulence-averaged two-phase flow modeling and the 3D LES approach in the present Eulerian two-phase modeling framework (Cheng et al., 2018) should be extended to simulate ripple regimes.

Data Availability Statement

The source code and the case setup to reproduce the same results are publicly available via the sedFOAM's official website http://servforge.legi.grenoble-inp.fr/pub/soft-sedfoam/

Acknowledgments
This study is supported by National Science Foundation (Grant no. OCE-1635151) and Strategic Environmental Research and Development Program (Grant no. MR20-1478). Numerical simulations presented in this study were carried out using the Caviness cluster at University of Delaware, and the Stampede2 cluster at the University of Texas at Austin via XSEDE. The authors are grateful to Dr. J. J. van der Werf for making his laboratory data available to us. The authors are also grateful to the developers involved in OpenFOAM, who are the foundation of the model presented in this paper.

References

Amos, C. L., Bowen, A. J., Huntley, D. A., & Lewis, C. F. M. (1988). Ripple generation under the combined influences of waves and currents on the Canadian continental shelf. *Continental Shelf Research*, *8*(10), 1129–1153. https://doi.org/10.1016/0278-4343(88)90016-7

Bagnold, R. A., & Taylor, G. (1946). Motion of waves in shallow water. Interaction between waves and sand bottoms. *Proceedings of the Royal Society of London. Series A, Mathematical and Physical Sciences*, *187*(1008), 1–18. https://doi.org/10.1098/rspa.1946.0062

Barr, B. C., Slinn, D. N., Pierro, T., & Winters, K. B. (2004). Numerical simulation of turbulent, oscillatory flow over sand ripples. *Journal of Geophysical Research*, *109*(9), 1–19. https://doi.org/10.1029/2002JC001709

Blondeaux, P., & Vittori, G. (1991). Vorticity dynamics in an oscillatory flow over a rippled bed. *Journal of Fluid Mechanics*, *226*(WW1), 257–289. https://doi.org/10.1017/S0022112091002380

Chang, Y. S., & Scotti, A. (2003). Entrainment and suspension of sediments into a turbulent flow over ripples. *Journal of Turbulence*, *4*, 1–22. https://doi.org/10.1088/1468-5248/4/1/019

Charru, F., & Franklin, E. M. (2012). Subaqueous barchan dunes in turbulent shear flow. Part 2. Fluid flow. *Journal of Fluid Mechanics*, *694*, 131–154. https://doi.org/10.1017/jfm.2011.528

Chauchat, J., Cheng, Z., Nagel, T., Bonamy, C., & Hsu, T. (2017). SedFoam-2.0: a 3-D two-phase flow numerical model for sediment transport. *Geoscientific Model Development*, *10*, (12), 4367–4392. https://doi.org/10.5194/gmd-10-4367-2017

Chauchat, J., & Médale, M. (2014). A three-dimensional numerical model for dense granular flows based on the μ(I) rheology. *Journal of Computational Physics*, *256*, 696–712. https://doi.org/10.1016/j.jcp.2013.09.004

Cheng, Z., Hsu, T. J., & Calantoni, J. (2017). SedFoam: A multi-dimensional Eulerian two-phase model for sediment transport and its application to momentary bed failure. *Coastal Engineering*, *119*, 32–50. https://doi.org/10.1016/j.coastaleng.2016.08.007

Cheng, Z., Hsu, T. J., & Chauchat, J. (2018). An Eulerian two-phase model for steady sheet flow using large-eddy simulation methodology. *Advances in Water Resources*, *111*, 205–223. https://doi.org/10.1016/j.advwatres.2017.11.016

Chen, X., & Yu, X. (2015). A numerical study on oscillatory flow-induced sediment motion over vortex ripples. *Journal of Physical Oceanography*, *45*(1), 228–246. https://doi.org/10.1175/JPO-D-14-0031.1

Chou, Y. J., & Fringer, O. B. (2010). A model for the simulation of coupled flow-bed form evolution in turbulent flows. *Journal of Geophysical Research: Oceans*, *115*(10), 1–20. https://doi.org/10.1029/2010JC006103

Clifton, H. E. (1976). Wave-formed sedimentary structures: A conceptual model. In R. A. DavisJr, & R. L. Ethington (Eds.), *Beach and nearshore sedimentation*. (Vol. *24*, pp. 126–148). Tulsa, OK: Society for Sedimentary Geology.

Clifton, H. E., & Dingler, J. R. (1984). Wave-formed structures and paleoenvironmental reconstruction. *Developments in Sedimentology*, *39*(C), 165–198. https://doi.org/10.1016/S0070-4571(08)70146-8

Crawford, A. M., & Hay, A. E. (2001). Linear transition ripple migration and wave orbital velocity skewness : Observations. *Journal of Geophysical Research*, *106*, 14113–14128.

Dimas, A. A., & Leftheriotis, G. A. (2019). Mobility parameter and sand grain size effect on sediment transport over vortex ripples in the orbital regime. *Journal of Geophysical Research: Earth Surface*, *124*(1), 2–20. https://doi.org/10.1029/2018JF004741

Ding, J., & Gidaspow, D. (1990). A bubbling fluidization model using kinetic theory of granular flow. *AIChE Journal*, *36*(4), 523–538. https://doi.org/10.1002/aic.690360404

Dong, P., & Zhang, K. (1999). Two-phase flow modeling of sediment motions in oscillatory sheet flow. *Coastal Engineering*, *36*(2), 87–109. https://doi.org/10.1016/S0378-3839(98)00052-0

Doucette, J. S., & O'Donoghue, T. (2006). Response of sand ripples to change in oscillatory flow. *Sedimentology*, *53*(3), 581–596.

Du Toit, C. G., & Sleath, J. F. A. (1981). Velocity measurements close to rippled beds in oscillatory flow. *Journal of Fluid Mechanics*, *112*, 71–96. https://doi.org/10.1017/S002211208100030X

Earnshaw, H. C., & Greated, C. A. (1998). Dynamics of ripple bed vortices. *Experiments in Fluids*, *25*(3), 265–275. https://doi.org/10.1007/s003480050229

Finn, J. R., Li, M., & Apte, S. V. (2016). Particle based modeling and simulation of natural sand dynamics in the wave bottom boundary layer. *Journal of Fluid Mechanics*, *796*, 340–385. https://doi.org/10.1017/jfm.2016.246

Gallagher, E. L. (2003). A note on megaripples in the surf zone: Evidence for their relation to steady flow dunes. *Marine Geology*, *193*(3), 171–176. https://doi.org/10.1016/S0025-3227(02)00662-X

Hsu, T.-J., Jenkins, J. T., & Liu, P. L.-F. (2004). On two-phase sediment transport: Sheet flow of massive particles. *Proceedings of the Royal Society of London. Series A, Mathematical, Physical and Engineering Sciences*, *460*(2048), 2223–2250. https://doi.org/10.1098/rspa.2003.1273

Hurther, D., & Thorne, P. D. (2011). Suspension and near-bed load sediment transport processes above a migrating, sand-rippled bed under shoaling waves. *Journal of Geophysical Research*, *116*(7), 1–17. https://doi.org/10.1029/2010JC006774

Jha, S. K., & Bombardelli, F. A. (2010). Toward two-phase flow modeling of nondilute sediment transport in open channels. *Journal of Geophysical Research*, *115*(3), 1–27. https://doi.org/10.1029/2009JF001347

Johnson, P. C., Nott, P., & Jackson, R. (1990). Frictional–collisional equations of motion for participate flows and their application to chutes. *Journal of Fluid Mechanics*, *210*, 501–535. https://doi.org/10.1017/S0022112090001380

Jones, K. R., & Traykovski, P. (2019). Interaction of superimposed megaripples and dunes in a tidally energetic environment. *Journal of Coastal Research*, *35*(5), 948–958. https://doi.org/10.2112/JCOASTRES-D-18-00084.1

Kim, Y., Mieras, R. C., Cheng, Z., Hsu, T.-J., & Puleo, J. A. (2018). Modeling sheet flow under breaking waves on a surf zone sandbar. *Coastal Engineering Proceedings*, *1*(36), 58. https://doi.org/10.9753/icce.v36.sediment.58

Li, M., Pan, S., & O'Connor, B. A. (2008). A two-phase numerical model for sediment transport prediction under oscillatory sheet flows. *Coastal Engineering*, *55*(12), 1159–1173. https://doi.org/10.1016/j.coastaleng.2008.05.003

Longuet-Higgins, M. S. (1981). Oscillating flow over steep sand ripples. *Journal of Fluid Mechanics*, *107*, 1–35. https://doi.org/10.1017/S0022112081001651

Marieu, V., Bonneton, P., Foster, D. L., & Ardhuin, F. (2008). Modeling of vortex ripple morphodynamics. *Journal of Geophysical Research*, *113*(9), 1–15. https://doi.org/10.1029/2007JC004659

Mogridge, G. R., Davies, M. H., & Willis, D. H. (1994). Geometry prediction for wave-generated bedforms. *Coastal Engineering*, *22*(3–4), 255–286. https://doi.org/10.1016/0378-3839(94)90039-6

Nagel, T., Chauchat, J., Bonamy, C., Liu, X., Cheng, Z., & Hsu, T. J. (2020). Three-dimensional scour simulations with a two-phase flow model. *Advances in Water Resources*, *138*, 103544. https://doi.org/10.1016/j.advwatres.2020.103544

Nelson, T. R., Voulgaris, G., & Traykovski, P. (2013). Predicting wave-induced ripple equilibrium geometry. *Journal of Geophysical Research: Oceans*, *118*(6), 3202–3220. https://doi.org/10.1002/jgrc.20241

Nichols, C. S., & Foster, D. L. (2007). Full-scale observations of wave-induced vortex generation over a rippled bed. *Journal of Geophysical Research*, *112*(10), 1–17. https://doi.org/10.1029/2006JC003841

Nielsen, P. (1981). Dynamics and geometry of wave-generated ripples. *Journal of Geophysical Research*, *86*(1), 6467–6472.

Nielsen, P. (1986). Suspended sediment concentrations under waves. *Coastal Engineering*, *10*(1), 23–31. https://doi.org/10.1016/0378-3839(86)90037-2

Nielsen, P. (1992). *Coastal Bottom Boundary Layers and Sediment Transport*. Indonesia: World Scientific.

Önder, A., & Yuan, J. (2019). Turbulent dynamics of sinusoidal oscillatory flow over a wavy bottom. *Journal of Fluid Mechanics*, *858*, 264–314. https://doi.org/10.1017/jfm.2018.754

O'Donoghue, T., Doucette, J. S., van der Werf, J. J., & Ribberink, J. S. (2006). The dimensions of sand ripples in full-scale oscillatory flows. *Coastal Engineering*, *53*(12), 997–1012. https://doi.org/10.1016/j.coastaleng.2006.06.008

Penko, A. M., Slinn, D. N., & Calantoni, J. (2011). Model for mixture theory simulation of vortex sand ripple dynamics. *Journal of Waterway, Port, Coastal, and Ocean Engineering*, *137*(5), 225–233. https://doi.org/10.1061/(ASCE)WW.1943-5460.0000084

Ribberink, J. S., van der Werf, J. J., O'Donoghue, T., & Hassan, W. N. M. (2008). Sand motion induced by oscillatory flows: Sheet flow and vortex ripples. *Journal of Turbulence*, *9*, 1–32. https://doi.org/10.1080/14685240802220009

Rodríguez-Abudo, S. & Foster, D. L. (2014). Unsteady stress partitioning and momentum transfer in the wave bottom boundary layer over movable rippled beds. *Journal of Geophysical Research: Oceans*, *119*(12), 8530–8551. http://dx.doi.org/10.1002/2014jc010240

Scheaffer, D. G. (1987). Instability in the evolution equations describing incompressible granular flow. *Journal of Differential Equations*, *66*(1), 19–50.

Sherwood, C. R., & Creager, J. S. (1990). Sedimentary geology of the Columbia River Estuary. *Progress in Oceanography*, *25*(1–4), 15–79. https://doi.org/10.1016/0079-6611(90)90003-K

Srivastava, A., & Sundaresan, S. (2003). Analysis of a frictional–kinetic model for gas–particle flow. *Powder Technology*, *129*(1–3), 72–85. https://doi.org/10.1016/S0032-5910(02)00132-8

Tjerry, S. & Fredsøe, J. (2005). Calculation of dune morphology. *Journal of Geophysical Research: Earth Surface*, *110*(F4). https://doi.org/10.1029/2004jf000171

Traykovski, P., Hay, A. E., Irish, J. D., & Lynch, J. F. (1999). Geometry, migration, and evolution of wave orbital ripples at LEO-15. *Journal of Geophysical Research*, *104*(C1), 1505–1524. https://doi.org/10.1029/1998JC900026

van der Werf, J. J., Doucette, J. S., O'Donoghue, T., & Ribberink, J. S. (2007). Detailed measurements of velocities and suspended sand concentrations over full-scale ripples in regular oscillatory flow. *Journal of Geophysical Research*, *112*(2), 1–18. https://doi.org/10.1029/2006JF000614

van der Werf, J. J., Ribberink, J. S., O'Donoghue, T., & Doucette, J. S. (2006). Modeling and measurement of sand transport processes over full-scale ripples in oscillatory flow. *Coastal Engineering*, *53*(8), 657–673. https://doi.org/10.1016/j.coastaleng.2006.02.002

Wengrove, M. E., Foster, D. L., Lippmann, T. C., de Schipper, M. A., & Calantoni, J. (2018). Observations of time-dependent bedform transformation in combined wave-current flows. *Journal of Geophysical Research: Oceans*, *123*(10), 7581–7598. https://doi.org/10.1029/2018JC014357

Wiberg, P. L., & Harris, C. K. (1994). Ripple geometry in wave-dominated environments. *Journal of Geophysical Research*, *99*(C1), 775–789. https://doi.org/10.1029/93JC02726

Yuan, J., & Wang, D. (2019). An experimental investigation of acceleration-skewed oscillatory flow over vortex ripples. *Journal of Geophysical Research: Oceans*, *124*(12), 9620–9643. https://doi.org/10.1029/2019JC015487

Zedler, E. A., & Street, R. L. (2006). Sediment transport over ripples in oscillatory flow. *Journal of Hydraulic Engineering*, *132*(2), 180–193. https://doi.org/10.1061/(asce)0733-9429(2006)132:2(180)

Zhou, J., Adrian, R. J., Balachandar, S., & Kendall, T. M. (1999). Mechanisms for generating coherent packets of hairpin vortices in channel flow. *Journal of Fluid Mechanics*, *387*, 353–396. https://doi.org/10.1017/S002211209900467X